(Received 1 August 2024, Accepted 14 September 2024, Scheduled 18 September 2024)

Alternative Plasmonic Materials for Biochemical Sensing: A Review

(*Invited Paper*)

Leonid Yu. Beliaev, Andrei V. Lavrinenko, and Osamu Takayama*

DTU Electro — Department of Electrical and Photonics Engineering
Technical University of Denmark, Ørsteds Plads 343, Lyngby, DK-2800 Kgs., Denmark

ABSTRACT: Optical materials whose permittivity becomes negative for certain wavelength ranges, so-called plasmonic materials, have been widely used for biochemical sensing applications to detect a wide variety of analytes from chemical agents to protein biomarkers. Since many analytes are or contain nanoscale objects, they interact very weakly with light. Thus, light confinement is a key to improving sensitivity. Using metal or plasmonic nanostructures is a natural solution to confine light and boost light-matter interactions. As there are several different optical sensing schemes, such as refractometric sensing, fluorescence-labeled sensing, and vibrational spectroscopy, whose operating wavelength spans from ultraviolet to mid-infrared wavelength regions, some plasmonic materials are superior to others for certain wavelength regions. In this article, we review current progress on alternative plasmonic materials, other than gold, silver, and aluminum, used in biochemical sensing applications. We cover a wide variety of plasmonic material platforms, such as transparent conductive oxides, nitrides, doped semiconductors, polar materials, two-dimensional, van der Waals materials, transition metal dichalcogenides, and plasmonic materials for ultraviolet wavelengths.

1. INTRODUCTION

Plasmonics is a sub-field of nanophotonics and optics, where electromagnetic fields are highly localized even below the diffraction limit and manipulated by metal (plasmonic) nanostructures, whose permittivities are negative [1, 2]. An interface between a metal and a dielectric is a typical example of a situation where the dielectric has a positive permittivity ($\epsilon_d > 0$) while the metal has a negative permittivity ($\epsilon_m < 0$). In such setting, surface plasmons are generated as oscillations of surface charge density in an electron-rich material, either confined inside structures like metal particles (so-called localized surface plasmons resonances or LSP resonances) or propagating on planar surfaces like thin metal films (known as surface plasmon polaritons, SPPs) [1]. Surface plasmons enable strong coupling of light to metal surfaces, leading to light confinement at nanoscale [3] and significant enhancements in light-matter interactions in the vicinity of metal nanostructures. Such features stimulate researchers to study plasmonics applications in a wide variety of areas in science and engineering, such as telecommunications [4], energy harvesting [5]. Furthermore, plasmonic materials are used as constituents of a wide variety of metamaterials and metasurfaces [6, 7], which support unique phenomena, such as negative refraction [8, 9], cloaking [10–14]. Apart from these applications, plasmonic nanostructures have been extensively used for biochemical sensing [15].

An optical sensor is an analytical tool that is capable of detecting and responding to physical input from its environment, converting it into a measurable optical signal [16]. Nowadays, plasmonic devices are widely commercialized as optical biochemical sensors [17–19]. Such sensors can be found in many fields, including medicine, environmental monitoring, and biotechnology. The challenge with optical sensing schemes is that many of the target analytes are extremely small, on the order of nanometers, and thus hard to detect due to the small interaction between probing light and the analyte. Highly confined light enabled by plasmons can address this challenge in the detection of nanoscale objects. For biochemical sensing applications, gold (Au) is the most popular choice of plasmonic materials thanks to its optical properties in the visible and near-infrared spectral range, chemical resistance, biocompatibility, and the well-known biofunctionalization process [18].

However, several significant drawbacks limit the use of metals, such as Au, Ag, Cu, and Al, as optical sensor materials. One of the most notable is optical losses due to a large imaginary part of metal's permittivity, which can lead to local heating of the structure, as well as broadening of plasmonic resonance, which is highly undesirable [20]. The local heating may result in detrimental effects, e.g., altering the refractive index of the surrounding medium, leading to false signals or inaccuracies in the measurements; non-specific binding; short-term stability; denaturation or structural changes in the target molecules, which directly affects the interaction between bio- or chemical compound and the sensing surface. Another issue is while gold is stable in the air, other metals, such as copper and silver, are susceptible to degradation due to oxidation and moisture [21, 22]. Additionally, some metals are incompatible with

* Corresponding author: Osamu Takayama (otak@dtu.dk).

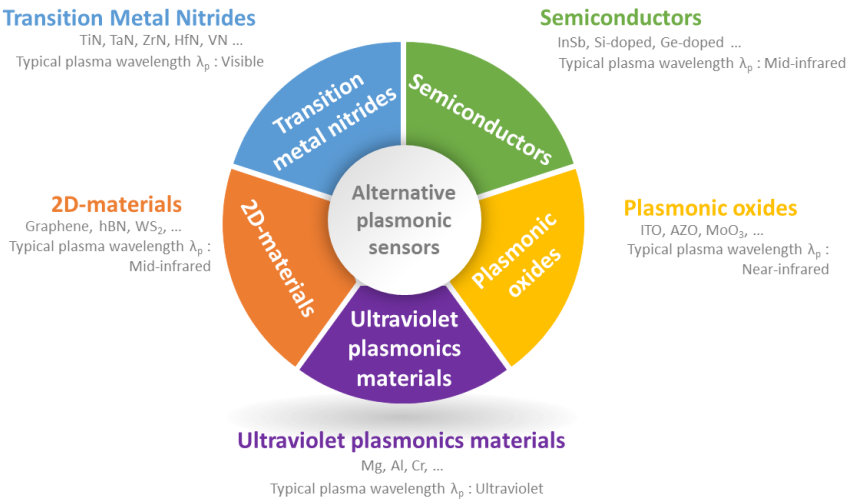

FIGURE 1. Different types of alternative plasmonic materials for biosensing applications.

standard complementary metal-oxide-semiconductor (CMOS) technology, compromising the scalability of sensing devices. Finally, these metals have difficulty in tuning their plasmonic properties (permittivity) [21, 22], while various optical sensing schemes span in a broad wavelength range from ultraviolet (UV) to mid-IR, or even to the THz regime.

To circumvent the challenges imposed by using conventional metals in sensing, two types of material platforms have emerged in the last decade: so-called "alternative plasmonic materials" and dielectrics. Alternative plasmonic materials here refer to materials that exhibit plasmonic behavior, similar to traditional noble metals like gold and silver [22] in the visible and near-infrared wavelength regions and beyond in other wavelength spectra in the UV and mid-IR regions. These alternative plasmonic materials include doped semiconductors, transition metal nitrides (TMNs), two-dimensional (2D) materials, transparent conductive oxides (TCOs), and so forth [22] (see Fig. 1). The main advantage of doped semiconductors, TMNs, and TCOs is that their plasmonic properties are tunable using various deposition parameters or doping levels [22]. In addition, some of them may possess better stability, lower cost, and CMOS compatibility [22, 23]. Moreover, 2D materials possess unique optical properties for certain wavelengths [24–28]. Recently, dielectric-based sensing platforms have been given big promises for their advantages, including low optical losses, avoided undesirable heating and narrow resonances allowing light to be localized for a long time with the increased intensity of the local field [29–36]. Some dielectric materials, such as silicon (Si), are also advantageous from the perspective of matured nanofabrication routines, enabling the realization of advanced structures and compatibility with the CMOS processes [37].

Up to present, there are numerous comprehensive reviews devoted to plasmonic predominantly gold-based sensing platforms [18, 38–43], as well as dielectric-based sensor platforms [36, 44–49]. There is also vast literature describing the optical properties of various groups of alternative plasmonic materials and their applications [22, 23, 50], including hybrid systems of 2D materials and metals [51–54]. However, there is a scarcity of reviews focusing on the employment of alternative plasmonic materials for biochemical sensing purposes apart from the terahertz frequency range [55]. Therefore, to fill the remaining niche in the field, this work aims to present recent advances in the application of different alternative plasmonic materials for optical sensing in the wavelength range from UV to mid-IR. This article is organized as follows. We start with the description of various types of major optical sensing schemes in Section 2. Section 3 introduces transition metal nitrides in optical sensing. In Section 4, we present an overview of sensing devices based on plasmonic oxides. The following Section 5 describes plasmonic materials for ultraviolet wavelengths. Doped semiconductors for mid-infrared absorption spectroscopy are discussed in Section 6. Section 7 is dedicated to plasmonic two-dimensional materials for sensing. Finally, Section 8 summarises the review and gives the outlook.

2. OPTICAL BIOCHEMICAL SENSORS

A typical sensor consists of three elements, a recognition element, a transducer, and a signal processor [56]. As a result of biological or chemical interactions of an analyte with the recognition element, the transducer part of the optical sensor relates the presence and concentration of the analyte to the variations in light properties, such as polarization, intensity, and wavelength [16], which are then converted to an electrical signal for further processing. There are different optical read-out schemes in the recognition element and transducer part of optical sensors, as illustrated in Fig. 2. All sensing schemes can be divided into two categories: label-based and label-free. Label-based optical sensors generate an optical signal by attaching special labels, such as fluorophores [57], quantum dots [58], nonlinear nanoparticles (NPs) [59]. Labels and working wavelengths are chosen based on such factors as sensitivity, target analyte, and background interference presented in the sensing environment [56]. One of the inspiring examples of the labeled method is fluorescence sensing, which is based on the registration of the

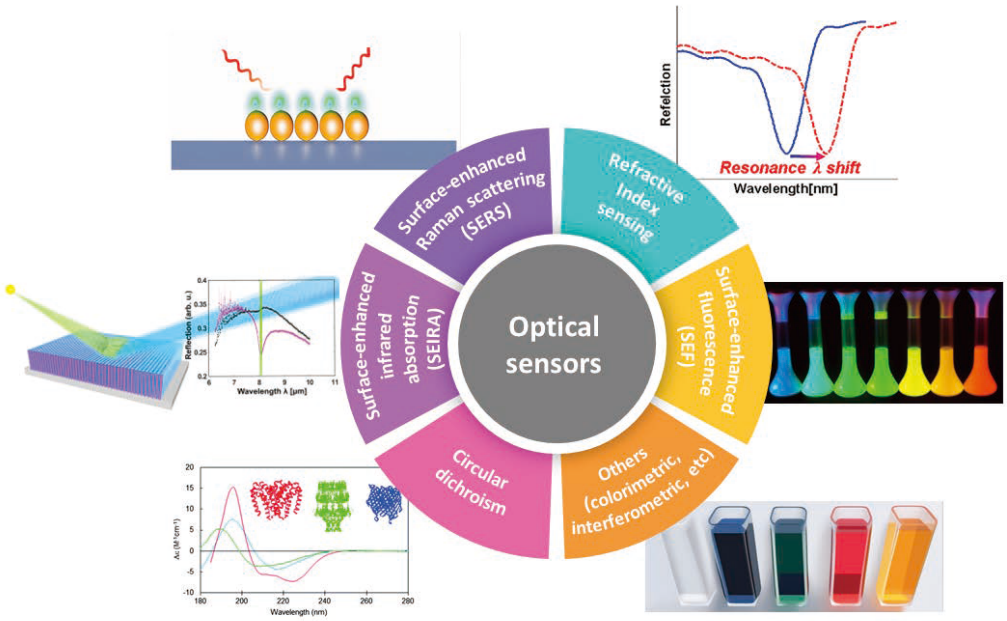

FIGURE 2. Different types of optical sensing schemes; refractometric sensing, surface-enhanced fluorescence (SEF) based on fluorescence sensing, surface-enhanced Raman scattering (SERS) based on Raman spectroscopy, surface-enhanced infrared absorption (SEIRA) based on infrared absorption spectroscopy, circular dichroism spectroscopy, and miscellaneous sensing techniques. Reproduced with permission [65–67].

fluorescent light intensity emitted by specific molecules (fluorophores) attached to an analyte of interest upon excitation on a specific wavelength. The advantages of fluorescence-based sensors are their high sensitivity, high selectivity, and rapid response [60]. However, its drawbacks include a weak signal with low analyte concentration, photobleaching, and autofluorescence [61]. To address the challenge of weak fluorescent signals, and increase fluorescence emission, plasmonic nanostructures with intense local electromagnetic fields that interact with proximal fluorophores were used [62]. The enhancement of fluorescence by plasmonic nanostructures is sometimes referred to as surface-enhanced fluorescence (SEF) [61, 63] and metal-enhanced fluorescence (MEF) [62, 64]. On the contrary, label-free sensing generates the optical signal by direct interaction with the analyzed material without a fluorescent label.

One example of a label-free technique is the refractometric or refractive index (RI) sensing used mainly for visible and near-IR wavelengths. In this case, the optical response or dispersion of modes (typically the position of the resonance in terms of wavelength or angle of incidence related to the wavevector) changes because of a variation in the refractive index of the surrounding environment in the vicinity of the sensor surface [36]. An important parameter describing the performance of this type of sensor is bulk-refractive index sensitivity (BRIS). This parameter shows how big is the resonance shift with a change in the refractive index of the background and is defined by [36]

$$S_B = \frac{\Delta\lambda}{\Delta n}\,[\text{nm/RIU}], \tag{1}$$

where $\Delta\lambda$ is the wavelength shift of the resonance induced by the change of the environment (bulk) refractive index Δn, and RIU is the acronym of a refractive index unit. The figure of merit (FOM) is another parameter for evaluating the performance of sensing structures. In FOM, the wavelength shift, $\Delta\lambda$, or bulk refractive index sensitivity, S_B, is related to the full width at half maximum (FWHM) of the resonance [36]:

$$\text{FOM} = \frac{S_B}{\text{FWHM}}. \tag{2}$$

In general, the narrower the resonance (FWHM), the better the accuracy in the small resonance shift distinction. Hence, a larger value of FOM is desirable.

In many biosensing applications, the nanometer scale analytes are immobilized on the sensor surface by a biofunctionalization layer designed to selectively capture the target analyte [18]. In such a situation, the refractive index change occurs only within a few nanometer distances from the surface in the constant refractive index background. Moreover, refractive indices of proteins, biomarkers and tissues, typically range from 1.4 to 1.6 [68–71] in the liquid background of water ($n = 1.33$), serum ($n = 1.35$), or phosphate-buffered saline (PBS, $n = 1.37$), making the refractive index contrast between the analyte and background small. These difficulties impose a technical challenge of refractometric sensing and require a highly localized electric field of plasmon modes to improve sensitivity. Surface sensitivity is defined by the wavelength shift of the resonance in terms of the thickness of the analyte layer on the sensor surface and is expressed by [72]

$$S_S = \frac{\Delta\lambda}{\Delta t}\,[\text{nm/nm, pm/nm}], \tag{3}$$

Surface sensitivity may be more relevant for the evaluation of the sensing performance than the BRIS detecting a nanometer-size analyte, such as proteins, captured on the sensor surface.

Additionally, the important parameter is the limit of detection (LOD), which represents the minimum concentration of the analyte that can be reproducibly detected [73, 74].

Hereby, we briefly discuss the photothermal effect of plasmonic nanostructures on sensors. Plasmonic materials are inherently lossy and prone to generate heat, resulting in temperature rise [75–77]. Depending on the irradiated power and plasmonic nanostructures, temperature increases range from several °C [78] to even a few hundred °C [79]. Local heating can result in changes in optical properties and false readings of optical signal changes, which are not caused by the presence of an analyte. For instance, the refractive index of distilled water can change 0.0001 at 633 nm in wavelength by merely 1°C of temperature variation [80]. This variation may result in critical errors for refractometric sensing. Therefore, care must be taken to circumvent the local heating effect of plasmonic nanostructures, and optical power needs to be sufficiently low to avoid the heating effect for visible and near-infrared wavelengths. In such a low optical power budget case, a narrower FWHM of resonance (larger quality factor) is required to maintain high sensitivity, as shown by periodic arrays of plasmonic particles that support lattice resonance [81]. Alternatively, dielectric-based periodic nanostructures, such as gratings, photonic crystals, metasurfaces, have been extensively studied recently [36]. These transparent dielectric systems support guided mode resonance, bound states in the continuum (BICs), or Mie resonance as field localization and sensitivity enhancement mechanisms instead of plasmonic resonances. The other advantage of dielectric platforms supporting guided mode resonance and BICs is their narrower resonance (high Q-factor), compared with plasmonic resonances.

Another family of label-free sensing schemes is vibrational spectroscopy, which includes Raman, IR absorption, circular dichroism (CD), and UV absorption spectroscopy. The Raman spectroscopy technique analyzes molecular vibration through molecular light scattering (Raman scattering). When photons interact with molecules, a part of their energy is transferred to the molecules. As a result, incident photons (typically in the visible to near-IR range) are scattered with lower energy (lower frequency or longer wavelength in the mid-IR range). This frequency is unique to the analyte molecules, enabling the identification of the molecules. Raman scattering provides information about the sample's chemical composition and structure [81, 82]. The infrared absorption method, on the other hand, relies on light absorption by molecules. The typical range of molecular absorption is in mid-IR with wavelengths between 2 and 20 μm (5000 and 500 cm^{-1}). The uniqueness of the molecular absorption bands allows for the identification of the chemical bonds and functional groups. These techniques have the same challenge of a weak optical signal that limits sensitivity, making it a critical problem in detecting biomarkers at low concentrations. Plasmonic nanostructures adoption ameliorated the challenges of the vibrational spectroscopy techniques, greatly enhancing Raman scattering and IR absorption. Such techniques modifications are referred to as the surface-enhanced Raman scattering (SERS) [81, 82] and surface-enhanced infrared absorption (SEIRA) [40, 83, 84], respectively.

The key performance parameter of these techniques is an enhancement factor (EF), the ratio between the signals (fluorescent emission, Raman signal, or infrared absorption signal) with and without nanostructures (enhancement mechanism),

$$EF = \frac{I}{I_0}, \tag{4}$$

where I and I_0 are, respectively, the signals with and without nanostructures (as the baseline). There are two kinds of EFs used in the assessment of performance: net or average enhancement factor, $\langle EF \rangle$, from the whole nanostructure which is measured experimentally, and local or peak enhancement factor, EF, which is usually calculated from numerical simulation on a hot spot where the localized electric field is the strongest [85]. Note that the SERS enhancement factor is proportional to $|E|^4/|E_0|^4$ [81], where E and E_0 are the local and incident fields, respectively, while in cases of SEIRA and SEF the enhancement factor depends on $|E|^2/|E_0|^2$ [61, 83]. The huge enhancement factor of SERS enables the identification of target analytes at low concentrations, or even up to the single molecule level [81]. SERS is used in a wide variety of biochemical and medical sensing [86], including cancer biomarker detection [87].

Circular dichroism (CD) spectroscopy operating in the wavelength range from the UV to mid-IR regions has been used to detect a wide variety of chiral molecules and chemical compounds. With the CD spectroscopy, one measures the difference in left- and right-hand circularly polarized light absorption by chiral molecules. The polarization-dependent absorption spectra provide identification of chiral molecules and their handedness, and the absorbance itself specifies molecular concentration. As many chiral drugs and proteins have CD absorption signals in the UV wavelengths, this technique is widely used in pharmaceutical and biopharmaceutical fields for drug discovery, analysis, optimization of chemical compounds, and production processes. The UV absorption spectroscopy detects absorption features of nucleotide bases and aromatic amino acids, such as adenine, thymine, guanine, cytosine, uracil, tryptophan, tyrosine below 300 nm wavelengths [88].

The optical sensing schemes and enhancement mechanisms, of course, are not limited to the mentioned above. There are other methods such as colorimetric, interferometric, and so on [16, 56]. Each method has its own advantages and disadvantages, and the choice of technique depends on the target analyte and required sensitivity. A variety of factors must be taken into consideration when it comes to the choice of sensing schemes. These factors include concentration, precision, sample volume, and detection time. In the review, we mainly cover refractometric sensing, SERS, SEIRA, and SEF.

3. TRANSITION METAL NITRIDES

One class of alternative plasmonics materials is so-called transition metal nitrides (TMNs), a group of chemical compounds made of transition metals and nitrogen [89, 90]. Recently, plasmonic properties have been described in such materials as titanium nitride (TiN) [91–94], zirconium nitride (ZrN) [95, 96],

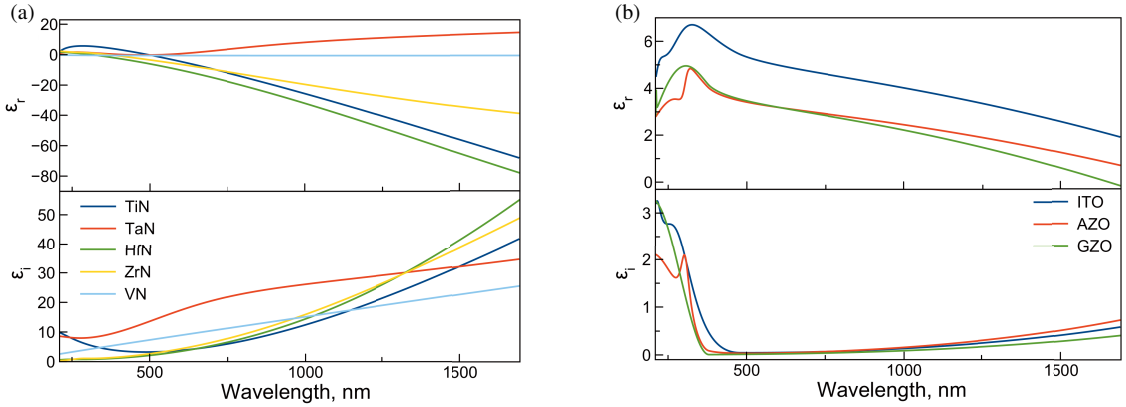

FIGURE 3. Real, ε_r, and imaginary part of permittivity, ε_i, of some (a) transition metal nitrides and (b) transparent conductive oxides. The thicknesses of the films are 70–100 nm. Experimental data obtained at DTU Nanolab, as well as from the literature [99, 103].

hafnium nitride (HfN) [97], tantalum nitride (TaN) [98], vanadium nitride (VN) [97, 99], tungsten nitride (WNx) [98], and niobium nitride (NbN) [100]. TMNs are highly advantageous due to their high melting points compared to noble metals, relative affordability, chemical robustness, high hardness and exceptional mechanical properties [89, 90]. Moreover, most of the TMNs are CMOS compatible [22]. These properties of TMNs find applications in catalysis [101], energy conversion [102], structural colors [103], photovoltaics [104], and photothermal applications [79].

Many TMNs possess negative real permittivities in the visible range and beyond, similar to Au and Ag [89] (see Fig. 3). Optical properties of such materials depend significantly on a deposition method, parameters, film thickness, and the substrate [22]. In addition, it is possible to tune the properties from metallic to dielectric and vice versa by making the material more metal- or nitrogen-rich [90]. One important consequence of optical tunability is the control of the transition wavelength, where the real part of the permittivity changes its sign. At this point permittivity becomes near zero, ($\varepsilon \approx 0$, so-called epsilon-near-zero (ENZ) material) leading to interesting effects, such as nonlinearity enhancement [105] and tunneling in waveguides [106]. By incorporating oxygen, it is possible to tune the double zero-crossover wavelengths of the ENZ points [94, 107]. Compared to other materials like transparent conductive oxides (TCOs), TMNs exhibit more significant losses associated with the imaginary part of the permittivity due to the larger Drude damping and interband losses [89, 108], as shown in Fig. 3. One way to reduce losses could be to use an appropriate substrate with the same or similar lattice constant as the deposited materials that supports the epitaxial growth of thin films with fewer defects acting as the scattering centers [22].

To a large extent, TMNs have found their application in different optical sensing schemes. For example, high aspect ratio TiN gratings were realized by deep reactive ion etching (DRIE) and atomic layer deposition (ALD) [109]. The structure supports a resonance at 705 nm at a 50-degree angle of incidence associated with the Rayleigh-Woods anomalies (RWAs). The measurements in distilled water ($n = 1.327$), ethanol ($n = 1.357$), and isopropanol ($n = 1.371$) provided BRIS $= 430$ nm/RIU. The same structures were also used to demonstrate the enhancement of infrared absorption of vanillin molecules in the mid-infrared region (around 6.6 µm) [110]. The enhancement occurs due to the strong electric fields produced by bulk plasmon modes within the gratings. In numerical study [111], different transition metal nitrides were evaluated for refractometric sensing scheme in the Kretschmann (prism coupling) configuration. These results revealed that TiN thin films demonstrated a better angular BRIS than ZrN one (22.28 deg/RIU against 21.34 deg/RIU).

Core-shell NPs covered by different TMN layers, such as TiN, ArN, HfN were theoretically analyzed in comparison with Au layers for refractometric sensing [112]. Conventional core-shell structures with the dielectric core covered by TMN layers and multilayered TiN core-shell NPs exhibit BRIS $= 203$ and 247 nm/RIU, outperforming ZrN and HfN ones. A theoretical work [113] proposes a design of titanium dioxide one-dimensional nanotube photonic crystal coated with a TiN layer. This structure supports a Fano resonance at 6.745 µm as a result of the interaction between the photonic crystal and TiN plasmonic modes. By optimizing the TiN plasmonic layer thickness, and geometrical parameters of the photonic crystal, BRIS $= 3798$ nm/RIU was reached. A sensor device that consists of a straight TiN-dielectric-TiN waveguide with embedded TiN dots and a square-ring resonator was proposed and numerically characterized using the Finite Element Method (FEM) [114]. The sensor exhibits a maximum sensitivity of 1074 nm/RIU and FOM $= 32.4$. Another interesting sensing platform is a photonic crystal fiber (PCF) whose external surface is coated with a TiN film to enhance its sensing capabilities [115–118]. The sensing principle is based on the fundamental fiber and plasmonic modes coupling. Any changes in the refractive index of the surrounding medium are reflected in the coupling strength. For instance, sensing performance for different operating wavelengths, TiN thicknesses, and channel widths was analysed [116], resulting in the BRIS up to 10000 nm/RIU. Besides, ZrN- and HfN-coated PCF's performance was compared with the Au-coated one [118]. The study showed that HfN- and ZrN-coated fibers outperform Au in visible in terms of BRIS (up to 8200 nm/RIU for HfN and

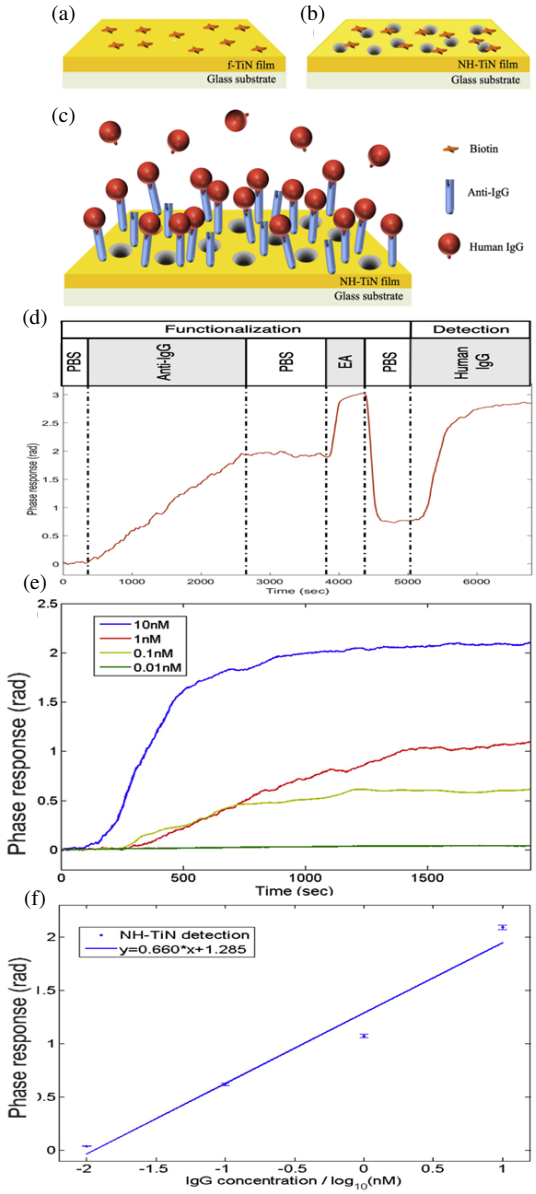

FIGURE 4. Biotin functionalization on (a) TiN thin film, and (b) TiN nanohole array. (c) Functionalization of human IgG for TiN nanohole array. (d) Functionalization and detection curve, (e) phase responce of IgG, and (f) IgG calibration curve. Reproduced with permission [125].

6800 nm/RIU for ZrN as opposed to 2300 nm/RIU of Au). This is directly connected with the lower losses (ϵ_2) of HfN and ZrN [119] than those of Au [120] in visible.

A 30 nm TiN polycrystalline film with dominant crystal orientation (200) was deposited by reactive magnetron sputtering [121]. The authors reported that the sample can be directly functionalized with biotin molecules without a linker (see Figs. 4(a), (b)). Biotin is widely used for functionalization procedures due to its strong and selective binding with avidin or streptavidin proteins, offering exceptional specificity, sensitivity, and versatility in detecting target molecules [122]. The adsorption mechanism of biotin on a TiN thin film was explored by density functional theory (DFT) simulations. It was revealed that there are contributions of two kinds: the carbonyl and carboxyl groups in biotin molecules exhibit a strong chemisorption on TiN surfaces through titanium-oxygen bonds, and the amines and sulfur compounds experience a weak physisorption via van der Waals force. In their subsequent work [123], the authors used functionalization with a biotinylated compound to quantitatively detect exosomes, which are extracellular vesicles isolated from a human glioma cell line. The LOD for exosomal membrane proteins was found to be 4.29 ng/mL for CD63, an exosome marker, and 2.75 ng/mL for epidermal growth factor receptor variant-III, a glioma-specific mutant protein. Moreover, the sensing performance of the TiN film compared with that of an Au film showed better sensitivity than the Au counterpart. The explanation of this fact is based on the interaction distances: biotin can be directly attached to the TiN surface, whereas, in the case of gold, an intermediate thiolates layer is needed. Therefore, in the former case, the biological target is closer to the surface, interacting stronger with the evanescent field of surface plasmon polaritons.

An air-holes array in deep-subwavelength gold (6 nm) on a TiN film was fabricated by a two-step fabrication method: first, by growing a high-quality two-phase (Au-TiN) vertically aligned nanocomposite template, followed by selective wet-etching of the metal (Au) [124]. The etching of Au can be controlled providing either fully etched Au in the holes or halfway etched. The structure exhibits two enhanced transmission peaks around 400–500 nm and 638–742 nm associated with surface plasmon resonances. The fully- and halfway etched structures were studied for enhancement of the 2D perovskite layer ($(C_6H_5CH_2CH_2NH_3)_2PbBr_4$) photoluminescence. The same sample was also probed for refractive index sensing showing BRIS $=$ 258 nm/RIU. Another TiN nanohole array was used as a biosensor to detect biotin molecules as an antibody, giving the LOD of 12.6 pM for human immunoglobulin G [125] (see Figs. 4(c)–(f)). A nanohole array in a TiN film on a SiO_2/Si stack exhibits a Fano-shape resonance, which position is sipping the wavelength range 980–1200 nm depending on the angle of incidence [126, 127]. The simulation revealed that the resonance results from the interference between plasmonic and Fabry-Pérot modes. By optimizing the nanohole array parameters as well as the thickness of the SiO_2 layer and angle of incidence, BRIS $=$ 2305 nm/RIU was achieved. A similar structure with a nanohole array in the TiN film on the SiO_2 substrate was studied [128], where plasmonic properties of TiN were tuned using reactive magnetron sputtering by varying Ar:N_2 gas ratio, demonstrating BRIS $=$ 180 nm/RIU. The article by Asencios et al., [129] describes the development of a biosensor based on the coupling of an SPP on a TiN film and a planar waveguide mode. The sensor is the analyte/Nb_2O_5/SiO_2/TiN/sapphire prism multilayer structure deposited by the DC magnetron sputtering. Using the Kretschmann configuration a bulk sensitivity was estimated as 30 degrees/RIU by measurements with three ambient media: air ($n = 1$), water ($n = 1.33$), and dried egg white ($n = 1.55$).

Interstitial metal nitrides have also been actively studied for SERS applications. For example, numerical analysis of NPs dimers for SERS substrates was carried out in [130–132]. In particular, the role of the sizes, embedding medium, and interparticle separations of ZrN and TiN NPs was studied in [130]. The study showed that ZrN NPs exhibit electric field inten-

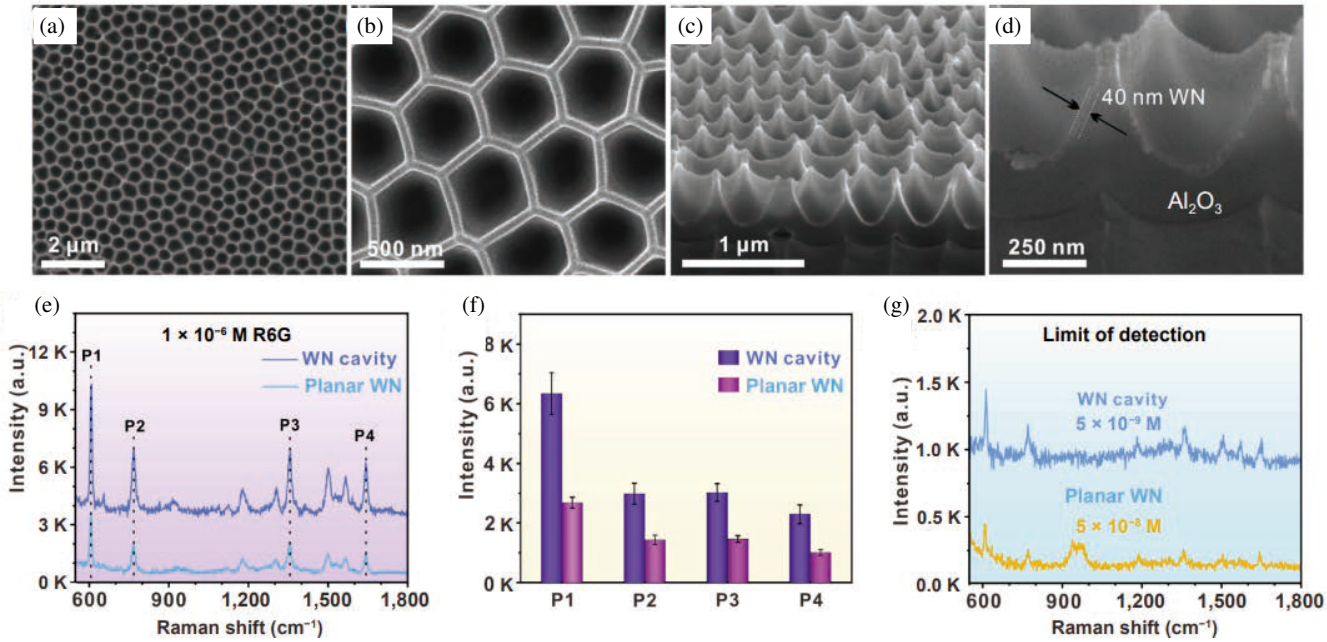

FIGURE 5. (a)–(d) The SEM images of WN nanocavity chips: (a), (b) the top view images; (c), (d) the cross-sectional images; (e), (f) the Raman spectra and corresponding signal intensity of 10^{-6} M R6G adsorbed on WN nanocavity and planar chips; (g) comparison of LOD of WN nanocavity and planar chips. Reproduced with permission [98].

sity enhancement similar to Au nanoparticles, while TiN NPs demonstrate less enhancement than both Au and ZrN NPs. TiN multimers were found to exhibit SERS enhancement of $\sim 1.9 \times 10^4$ and BRIS $= 127$ nm/RIU [131]. Similarly, TiN nanodonuts with LSP resonances in visible and near-infrared were studied in [132]. By optimizing geometrical parameters, the BRIS and SERS enhancement factor reached 1374 nm/RIU and 6.8×10^4, respectively. Sputtered HfN [133] and TiN [134] thin films were studied in SERS applications. A HfN thin film exhibits $EF = 8.5 \times 10^4$ to methylene blue (MB) molecules [133], while $EF = 6.2 \times 10^3$ and $EF = 1.3 \times 10^4$ were demonstrated for the flat and wrinkly TiN films [134]. TiN thin films were made by direct nitridation of a sol-gel derived TiO_2 thin films at different temperatures in ammonia gas [135]. The films showed improved SERS performance as the nitridation temperature increased due to changes in composition, microstructure, and optical properties. SERS performance of WN and TaN thin films were studied in [98]. These films demonstrated SERS EFs around 10^5 due to the efficient photoinduced charge transfer process between films and probed molecules. To improve the SERS properties further, WN hexagonal arrays were characterized (see Figs. 5(a)–(d), giving an additional 2.2 times enhancement in comparison with pristine planar films. Rhodamine 6G (R6G) LOD $= 5 \times 10^{-9}$ M was reported (see Figs. 5(e)–(g)). WN/monolayer MoS_2 (W/M) vertical heterostructures were fabricated in this work as well. The Raman spectra and mapping intensities demonstrate higher SERS signals on the W/M chips. The fluorescence quenching of MoS_2 suggests efficient charge transfer between MoS_2 and WN, contributing to the enhanced Raman scattering cross-section.

ZnO nanowire arrays decorated with TiN NPs with 30–100 nm sizes were studied in [136] as a SERS substrate. The TiN NPs were produced by grinding commercially obtained TiN powders and then dispersed on ZnO nanowires by drop casting. The TiN-decorated ZnO nanowires exhibit SERS enhancement using Nile blue and MB as the analyte molecules. The origin of the enhancement effect involves surface plasmon and adsorbed molecule resonances, and charge transfer. A TiN nanorod array was studied as another potential SERS platform [137, 138]. Such structure was prepared using the glancing angle deposition in a magnetron sputtering system [137]. The $EF = 10^4$ for an R6G concentration of 10^{-6} M was observed. A hydrothermal process followed by nitridation in an ammonia atmosphere was used to fabricate TiN nanorod arrays in [138]. The samples prepared at 900°C were found to exhibit the strongest Raman enhancement factor of 8.9×10^3 and LOD $= (10^{-6}$ M) for R6G and crystal violet (CV) as probe molecules, while the R6G molecules can have a higher enhancement than the CV ones. Furthermore, suspensions of TiN NPs were prepared using nanosecond Ce:Nd:YAG pulsed laser ablation of a TiN target immersed in various solvents [139]. The NPs, being characterized by various spectroscopic, structural, and compositional analysis techniques, display strong optical absorption in the near-IR range. When the diameter of plasmonic (metal) NPS is a lot smaller than the wavelength, ***LSP*** is supported under the condition that the real part of permittivity becomes $\mathrm{Re}(\varepsilon_m(\omega)) = -2\varepsilon_d$, where ε_m and ε_d are the permittivities of metal and dielectric, respectively [2]. The TiN NPs were then used as the SERS substrates for MB molecules, resulting in a similar to other above-mentioned SERS substrates EFs.

Transition metal nitrides have also been used for fluorescence enhancement [140–142]. A TiN thin film on a glass substrate was demonstrated to support surface plasmon-coupled emission similar to conventional Au films [140]. By integrating different fluorophores, e.g., Nile Red (NR) and 5,10,15,20-tetrakis(4-Nmethylpyridyl)porphyrin (TMPyP) with TiN-based substrates, as the study showed, directional fluorescence emission got tunable possibilities, highlighting TiN's potential as a SEF-platform. ZrN nanoparticles in a square array were coated with 600 nm thick PMMA containing R6G fluorescent molecules [141]. The net $EF = 9.7$ was demonstrated compared with the bare glass substrate. This is higher than the value achieved for the similar periodic array of TiN nanoparticles (2.8 times enhancement) demonstrated earlier by the same group [142].

4. PLASMONIC OXIDES

4.1. Transparent Conducting Oxides

Another group of alternative plasmonic materials is formed by transparent conducting oxides (TCOs) [22]. Such oxides as indium oxide, zinc oxide, and cadmium oxide can be highly n-doped to make them conducting, while still being transparent in the visible wavelength range [50]. Unlike TMN materials exhibiting plasmonic properties in the visible range, TCOs, due to the lower carrier concentrations, have conventionally plasmonic behavior in the near-IR range. The latter also may lead to significantly lower losses, for instance, five times less than silver films in certain ranges [22, 143]. Just like TMNs, TCOs also have excellent tunability of their optical properties and ENZ points by adjusting doping and deposition parameters [50]. In addition, these properties depend on the sample thickness mainly due to defects within the film and substrate interface that can trap carriers [144–146].

Due to their unique combination of properties such as transparency and conductivity, TCOs find applications in many areas. One example is in display panels, where they form the electrical contacts to the pixel circuit [89]. Moreover, the zero-crossing point of such materials could be adjusted to the telecommunication wavelengths leading to enhanced light-matter interactions [50, 106]. In addition, transparent conductive oxides can work as efficient absorbers in the mid-IR region [147]. TCOs are also used for sensing. For example, doped zinc oxide (ZnO) is often incorporated in gas-sensing devices with electrical read-out where changes in the material's resistivity in contact with gas molecules are detected. Since only optical methods of signal detection are considered in this paper, the above-mentioned electrical gas sensors are beyond the scope of this review, and interested readers can find information elsewhere [148, 149]. In addition, only plasmonic sensors are considered here. However, apart from plasmonic sensors, there are works where conductive oxides were used, for example, as a hybrid (metal-dielectric) systems [150], optical fibers that support surface plasmons [151, 152] and lossy mode resonances [153–155], gratings supporting guided-mode resonances [156] and Fabry-Pérot resonances [157], and photoluminescence sensors [158, 159].

TCO-based sensors have been demonstrated for gas detection. For instance, a series of work has been done related to a fiber-optic ammonia gas sensor [160–162]. The device was made by removing a section of the fiber cladding and depositing thin layers of ITO and polyaniline [160, 161] or bromocresol purple (BCP) [162] on the exposed surface. The sensor works by using intensity modulation and wavelength interrogation methods and is capable of detecting gas in the concentration range of 10–150 ppm [160, 161] and 1–10 ppm [162], respectively. Moreover, it showed that the sensitivity and operating range of the sensor depends on the thickness of the ITO layer.

Besides ammonia, another gas of close interest is hydrogen (H_2), a highly combustible gas that can easily explode in concentrations over 4%. Aluminum-doped ZnO (AZO) particles-based films were used for H_2 gas sensing [163]. Upon exposure to reducing gas species of H_2 at 500°C, a reduction in transmission at longer wavelengths ($\lambda > 2200$ nm) and an increase in transmittance for intermediate wavelengths ($\lambda \sim 1500$–2200 nm) was observed, which is reversible. Theoretical analysis suggests that the near-IR absorption and changes in optical spectra are caused by modifications in the free carrier density through high-temperature gas atmosphere exposure. ZnO nanocrystals doped with gallium (GZO), aluminum (AZO), and germanium (GeZO) were used as H_2 and nitrogen dioxide (NO_2) gas sensors [164]. By a non-aqueous colloidal heat-up synthesis process, nanocrystals with adjustable dopant concentration were synthesized with high transparency in the visible range and strong LSP resonances in the near-infrared. These nanocrystals detect both gases at mild (above 100°C) operating temperatures with sub-ppm LOD. The summary of plasmonic TCO and TMN structures for refractometric sensing is given in Table 1. As can be seen from the results, sensitivity can vary greatly, depending on the structure and fabrication method.

Since the plasmonic behavior ($\mathrm{Re}(\varepsilon) < 0$) of these TCO materials extends from near-IR to mid-infrared (MIR) wavelengths, they can be employed in SEIRA applications. For example, ITO nanorod arrays were demonstrated for protein detection [170]. The single crystalline ITO nanorods, fabricated on an yttrium-stabilized zirconia (YSZ) substrate by a combination of epitaxial growth, electron beam lithography (EBL), and reactive ion etching [171], exhibit two incident angle-dependent plasmon resonances. The ITO nanorod surfaces were functionalized by phosphonic-acid-derived biotin molecules with a strong affinity toward streptavidin. Vibration signals of the amide-I (at 6.0 µm or 1660 cm^{-1}) and amide-II (at 6.5 µm or 1537 cm^{-1}) from the biotin-streptavidin bondings were amplified by two plasmon modes supported by the ITO nanorod array. AZO high aspect ratio nanotrench structures [172–174] (see Figs. 6(a)–(c)) were probed for SEIRA applications to detect nanometers-thick silica films as model analyte with an absorption band around 8 µm [65].

Ga-doped ZnO (GZO) nanoparticles that support SPR were used as SERS substrates for 4-mercaptopyridine molecules [175]. Nanoparticles were prepared using the sol-gel method. The structures exhibited SPRs in the visible, near- and mid-IR regions. The enhancement factor of GZO

TABLE 1. Summary of plasmonic TCO and TMN materials for refractometric sensing and 2D TMO for absorption-based and refractometric sensing from visible to near-IR wavelengths. ALD: atomic layer deposition. evap.: evaporation. RF-sput.: Radio-frequency sputtering. IgG: Immunoglobulin G. CD63: exosome marker. EGFRvIII: epidermal growth-factor receptor variant-III. DC-sput.: direct current sputtering; PLD: pulsed laser deposition. ″: same as above.

Material/structure	Deposition/fabrication	Interrogation scheme	Analyte	Sensitivity/LOD	Ref.
TCO					
AZO tubes	ALD	Wavelength	H_2 gas	0.2–4.0%	[157]
TMN					
TiN thin film	RF-sputtering	Wavelength	Biotin	264 nm/RIU 0.22 μg/mL	[121]
″	″	″	CD63 EGFRvIII	4.29×10^{-3} μg/mL 2.75×10^{-3} μg/mL	[123]
TiN nanohole array	RF-sputtering	″	IgG	12.6 pM	[125]
″	Sputtering	″	–	2305 nm/RIU	[126, 127]
″	Sputtering	″	–	180 nm/RIU	[128]
TiN waveguide	DC-sputtering	Angle	–	30°/RIU	[129]
″	PLD	Wavelength	–	259 nm/RIU	[124]
TiN trenches	ALD	″	–	430 nm/RIU	[109]
TMO					
MoO_3 nanoflake	Exfoliation	Absorption	BSA	–	[165]
MoO_3 nanosheet	Oxidation of MoS_2	″	″	–	[166]
α-MoO_{3-x} nanoflakes on microfiber	Exfoliation	″	″	1 pg/mL	[167]
H_xMoO_3 nanodisk	Hydro-thermal synthetic methods	″	Glucose	2 nM	[168]
″ on Si microring resonator	″	Wavelength	pH	0.32 ± 0.02 nm/pH	[169]

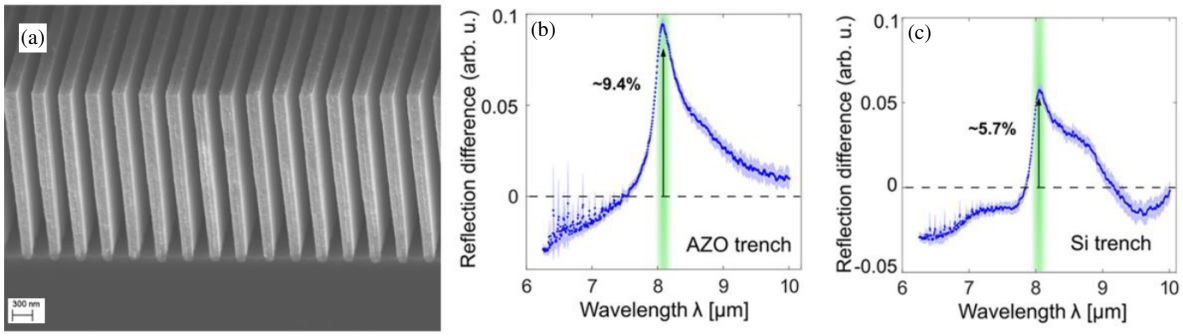

FIGURE 6. AZO metasurfaces for mid-IR absorption sensing. (a) The SEM image of the nanotrench structure and vibrational signal of (b) SiO_2 layer as analyte using plasmonic AZO gratings, compared with (c) dielectric Si ones. Reproduced with permission [65].

substrates ranged from 4.65×10^3 to 6.66×10^4 depending on the doping ratios (5% showed the best improvement), excitation wavelengths, and the presence of SPRs near the excitation wavelength.

Photonic crystal fibers (PCFs) functionalized by TCOs are another conventional type of optical sensors [176–179]. A PCF device operating in the 1.5–2.5 μm range was made from ITO as a plasmonic material. Its detection capability was improved by an additional layer of graphene because of its excellent molecular adsorption [176]. Numerical simulations demonstrated a BRIS of up to 12000 nm/RIU. Another ITO-coated fiber working in the same wavelength range was reported to have BRIS of 2000–15000 nm/RIU [177]. An AZO-coated PCF with BRIS of 1750 and 1950 nm/RIU was theoretically studied in [178]. A graphene/ITO nanorod metamaterial-based U-bent optical fiber was devised in [179]. This sensor consists of ITO nanocolumn array coated with graphene, allowing it to exert a significant bulk plasmon resonance effect. Using different alcohol solutions, a BRIS of the device was experimentally estimated as 690 nm/RIU. The device showed good specificity, and the ability to detect the target DNA probe at sub-nanomolar concentrations.

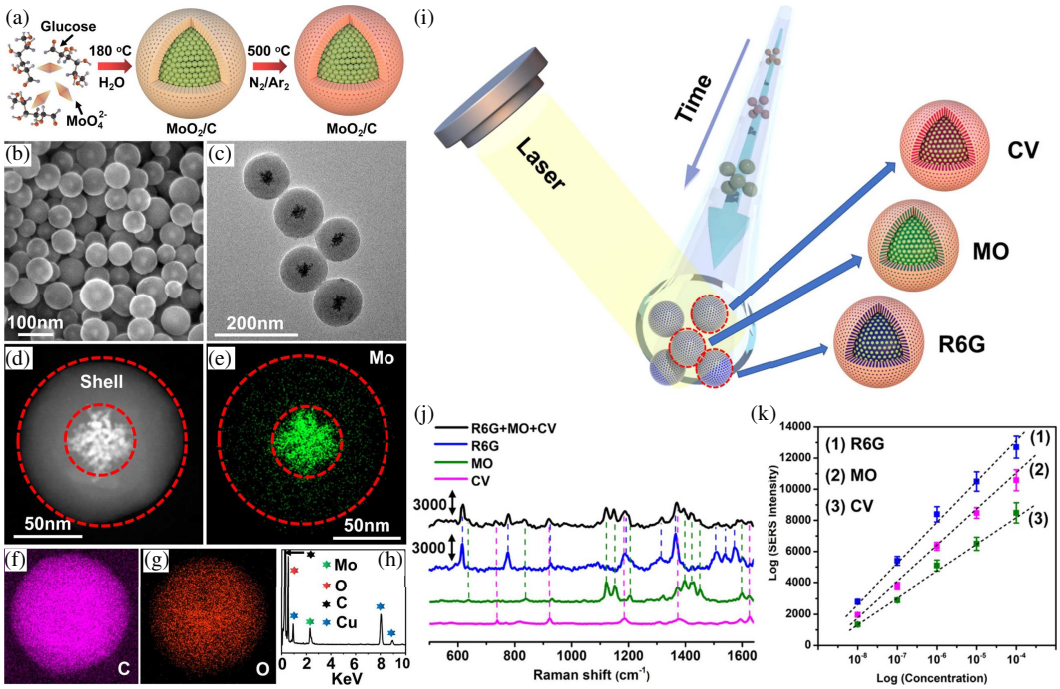

FIGURE 7. (a) MoO_2/C nanosphere synthesis scheme. (b) The SEM image. (c) The TEM image. (d) High-angle annular dark-field (HAADF) image. (e)–(h) Energy-dispersive spectrometry (EDS) mapping and spectrum. (i) Multi-component sample detection schematic. (j) The SERS spectra of the analyte samples are shown in single and multiplex formats. (k) Relationship between the signal intensity and sample concentration. Reproduced with permission [186].

4.2. Transition Metal Oxides

Apart from TCOs, there is another group of doped oxides with plasmonic properties, so-called transition metal oxides (TMOs) [180]. While some of them can be more or less transparent, they are not commonly used as transparent conductive materials in the same manner as conventional TCOs. Examples of such materials are molybdenum oxide (MoO_3) [181], tungsten oxide (WO_3) [182], titanium dioxide (TiO_2) [183] and so on. Depending mainly on doping, the plasmonic behavior of TMOs can vary greatly in the range from 500 nm to 3000 nm and beyond [180]. Several reviews describe the use of these materials [180, 184, 185]. Here we focus on TMO-based nanostructures as SERS platforms and 2D TMOs materials in sensing applications.

Plasmonic molybdenum dioxide-carbon composite (MoO_2/C) nanospheres were utilized for microfluidic detection of various analytes by SERS (R6G, MB, methyl orange (MO), and CV) (see Fig. 7) [186]. The nanospheres possess a super hydrophilic surface that can anchor analytes while avoiding contamination of the detection channel. The extreme LOD up to 10^{-12} M and EF 6.3×10^8 in the R6G detection were achieved. MoO_2 nanospheres are synthesized through a hydrothermal method [191], giving LOD of 10^{-8} M and a significant enhancement factor of 4.8×10^6 for R6G. Such nanospheres also exhibit excellent stability, with resistance to corrosion from strong acids and alkalis, as well as high-temperature oxidation. MWO nanoparticles were synthesized by a one-pot solution strategy [188]. The experiment demonstrates that the structures $EF = (6.09 \times 10^7)$, and LOD in the detection of R6G is 10^{-8} M. The observed enhancement of the SERS performance was attributed to the cumulative effect of the charge transfer and the plasmon resonance. $W_{18}O_{49}$ nanowires were probed as a SERS platform too [189]. When the nanowires aggregate, the ***LSP*** resonance peaks shift from near-IR to the visible wavelengths. The study focuses on oriented $W_{18}O_{49}$ bundles and dispersed nanowires with ***LSP*** resonances at 561 nm and 1025 nm, accordingly. The oriented nanowire bundles exhibit significantly higher SERS sensitivity than the randomly dispersed ones. The sensitivity enhancement is attributed to the synergistic effect of ***LSP*** coupling among the oriented ultrathin nanowires and oxygen vacancy-assisted charge transfer. In addition, the following structures were investigated as platforms for efficient SERS: Mo/MoO_2 nanospheres [192] (concept includes combining Mo nanoparticles with plasmonic MoO_2), MoO_2 nanowires [190], h-MoO_{3-x} and α-MoO_{3-x} nanoparticles [181], oxygen-deficient MoO_{3-x} nanosheets [187]. A comparison of the SERS performance of TMOs and other structures is presented in Table 2. As presented, the enhancement factor can vary by several orders of magnitude depending on the materials and structure shape.

Plasmonic 2D molybdenum oxide (MoO_3) was also demonstrated for biosensing applications in visible and near-IR regions [165–169]. Molybdenum oxide nanoflakes were exfoliated, using grinding-assisted sonication in various mixtures of water with protic and aprotic solvents [165] where the choice of solvent mixture influenced the thickness, lateral dimensions, and yield of the nanoflakes due to the effects of surface en-

TABLE 2. Comparison of different alternative plasmonic materials as SERS-platform. 4MPy: 4-mercaptopyridine. EF: enhancement factor. LOD: limit of detection. MB: methylene blue. R6G: rhodamine 6G. TMN: transition metal nitrides. TCO: transparent conductive oxides. TMOs: transition metal oxide. ″: same as above.

Material	Structure	Excitation wavelength [nm]	Analyte	EF	LOD	Ref.
TMN						
TiN	Nanorods	532	R6G	8.9×10^3	1.0 μM	[138]
″	Thin film	″	″	1.3×10^4	-	[134]
″	Nanorods	″	″	1.0×10^4	1.0 μM	[137]
″	Multimers	″	-	1.9×10^4	-	[131]
″	Nanodonuts	633, 785, 980, 1064	-	6.8×10^4	-	[132]
HfN	Thin film	632	MB	8.5×10^4	-	[133]
WN	″	532	R6G	6.7×10^5	50 nM	[98]
TaN	″	″	″	6.7×10^5	500 nM	
Mo_2N	″	″	″	6.7×10^5	10 nM	
WN	Hexagonal array	″	″	1.9×10^7	0.5 nM	
TCO						
GZO	Nanoparticles	488, 532, 633, 785	4Mpy	6.6×10^4	-	[175]
TMO						
MoO_{3-x}	Nanosheets	514.5	R6G	1.0×10^{10}	0.3 fM	[187]
MWO	Nanoparticles	532	″	6.0×10^7	10 nM	[188]
$W_{18}O_{49}$	Nanowires	″	″	2.8×10^7	100 nM	[189]
MoO_2	″	″	″	2.9×10^7	10 pM	[190]
MoO_2	Nanoparticles	″	″	4.8×10^6	10 nM	[191]
h-MoO_3	″	632.8	MB	6.9×10^5	1.0 nM	[181]
αMoO_3	″	″	″	8.5×10^5	100 nM	
MoO_2/Mo	″	532	R6G	6.2×10^7	100 pM	[192]
MoO_2/C	″	″	″	6.3×10^8	1.0 pM	[186]

ergy and solubility. The samples exhibit two plasmon resonance peaks (around 650 and 950 nm), which could be tuned by selecting specific solvents in the exfoliation process. Bovine serum albumin (BSA) was exploited as a model protein analyte in sensing tests. The immobilized BSA molecules that are negatively charged repel the free electrons on the nanoflake surface, decreasing the free electron density near the surface of the flakes and changing the plasmonic peak intensity. The same scheme of BSA sensing was conducted for MoO_3 nanosheets made by combining the oxidation of MoS_2 and subsequent treatment with supercritical CO_2 [166].

Alpha-phase MoO_3 (α-MoO_3) nanoflakes were integrated onto optical microfibers as sensing cells [167]. α-MoO_3 flakes were heavily doped with free electrons through H^+ intercalation, resulting in a plasmon resonance at around 735 nm. This hybrid platform detected the BSA concentrations as low as 1 pg/mL. Another hybrid system, which consists of a Si microring resonator coupled with a 2D plasmonic molybdenum oxide layer, was demonstrated for pH sensing [169]. Hydrogen-doped molybdenum oxides (H_xMoO_3) nanodisks with 2D morphology were investigated too [168]. It turned out that the plasmonic features of H_xMoO_3 are significantly altered based on the intercalated H^+ concentrations. This behavior was demonstrated with an enzymatic glucose sensing model, where the enzymatic oxidation of glucose generates H_2O_2. The biochemical reaction causes rapid changes in the H^+ dopant levels and leads to large modulations in plasmonic properties. The optimal sensing response is achieved with the specific intercalated H^+ concentration, leading to the LOD of 2 nM. Interesting that α-MoO_3 becomes a biaxial hyperbolic material with one of permittivity tensor components being negative in the mid-IR region between 9.9 and 18.3 μm (1010–545 cm^{-1}) [193].

5. ULTRAVIOLET PLASMONICS MATERIALS

The ultraviolet region with wavelengths below 400 nm is a playground for various biochemical sensing and imaging routines, such as UV absorption spectroscopy, autofluorescence microscopy [194], circular dichroism (CD) spectroscopy, Raman spectroscopy, and imaging, as illustrated in Fig. 8. Moreover, when excited by UV light at 260–300 nm, biomolecules can fluoresce in 300–700 nm without a fluorescent label. This phenomenon is called autofluorescence. It takes place in more than 90% of all known proteins containing tryptophan, tyrosine, and phenylalanine [194, 195]. The autofluorescence eliminates the need for attaching fluorescence dye molecules. However, the autofluorescent and CD absorption signals are weak, requiring pronounced enhancement in potential applications. This is where plasmonic materials and nanostructures can contribute with LSP resonance for UV region wavelengths down

TABLE 3. Summary of alternative plasmonic materials for ultraviolet wavelengths and their sensing applications. ALD: atomic layer deposition. AN: ammonium nitrate. AO: Acridine orange. CFV: cresyl fast violet. Colorim.: Colorimetric sensing. CS124: carbostyril 124. CV: crystal violet. DMSO: dimethyl sulfoxide. DNT: 2,4-dinitrotoluene. EB evap.: electron beam evaporation. EF: local/peak enhancement factor. $\langle EF \rangle$: average/net enhancement factor. FIB: focused ion beam. H. pylori: Helicobacter pylori. LOD: limit of detection. NC: nanocube. RF-sput.: radio-frequency sputtering. PATP: p-aminothiophenol. PLD: pulsed laser deposition. PNBA: p-nitrobenzoic acid. Refract.: refractometric sensing. S101: Sulforhodamine 101 fluorophore. SA: streptavidin. SEF: surface-enhanced fluorescence. SERS: surface-enhanced Raman spectroscopy. SF: sodium fluorescein. Sput.: sputtering. ″: same as above.

Material/structure	Deposition/fabrication	Sensing technique	Analyte/excitation wavelength	Sensitivity/LOD/EF	Ref.
Mg nanohelix	EB evap.	Refract.	DMSO	–	[206]
″ nanohole array	Sput., FIB	SEF	P-terphenyl dye	$\langle EF \rangle$: 7.2	[207]
″ discs	Nano-imprinting	Colorim.	Humidity, sweat	50–95%	[208]
Rh spheroids	Electrochemical	SERS	Pyridine @ 325 nm	EF: ~ 100	[209]
″ nanotripods	Polyol method	″	PATP @ 325 nm	EF: 4.5	[210]
″ NCs	″	″	″	EF: ~ 400	[211]
″ concave NCs	″	″	PNBA @ 266 nm,	LOD: 10^{-10} M	[211]
			DNT,	LOD: 10^{-7} M	
			AN	LOD: 10^{-12} M	
″ NCs	″	SEF	PATP @ 266 nm, SA, hemoglobin @ 295 nm	$\langle EF \rangle$: 120	[212]
In NPs with silica shell	Polyol method	SEF	CS124 @ 350 nm, tryptophan @ 280 nm	$\langle EF \rangle$: 2–3 $\langle EF \rangle$: 5–7	[214]
″ NPs	Thermal evap.	SERS	Adenine @ 266 nm	EF: 11	[215]
Ga NPs	MBE	SERS	CV dye @ 325 nm	EF: $\sim 10^7$, $\langle EF \rangle$: 5–22	[216]
		SEF		$\langle EF \rangle$: 2–9	
″	Thermal evap.	Refract.	H. pylori	LOD: 10 pM	[217]
″	″	″	″	LOD: 6.0 pM	[218]
Si NPs, air hole array in Si	Theory	″	–	190 nm/RIU	[219]
Si, Ge, GaAs triangular NPs	Theory	″	–	75, 100, 215 nm/RIU	[220]

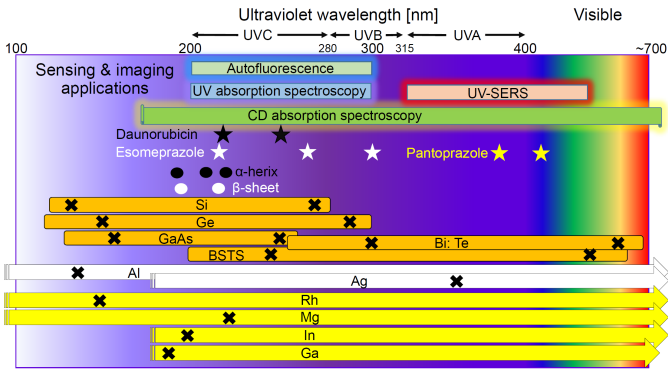

FIGURE 8. Alternative plasmonic materials for ultraviolet wavelengths where permittivity becomes negative, as well as wavelength ranges of applications. Note that $\times$ represents the approximate resonant wavelength (Fröhlich wavelength at which $\mathrm{Re}(\varepsilon) = -2\varepsilon_d$, where $\varepsilon_d = 1$ for nanoparticles. $\star$ indicate the position of CD signal peaks of some exemplary chiral molecules and drugs, such as daunorubicin (anticancer drug) [203], esomeprazole and pantoprazole (drugs to reduce stomach acid) [204], and $\bigcirc$ are for α-helix and β-sheet, which are building blocks of proteins [67, 205]. BSTS: $Bi_{1.5}Sb_{0.5}Te_{1.8}Se_{1.2}$.

to 200 nm [196, 197]. Conventionally, aluminum (Al) has been extensively used as a plasmonic material for its short plasma wavelength and low loss in the deep UV regime. Al plasmonic applications in UV include SERS [88, 198–200], autofluorescence enhancement [195, 201], label-free autofluorescent imaging [201], and surface-enhanced fluorescence (SEF) by long-range surface plasmons at 204 nm wavelength [202]. However, Al-based nanostructures can be oxidized, degrading LSP properties, and especially diminishing the SERS enhancement ability. This fact calls for Al substitution with alternative plasmonic materials for this wavelength region.

Interestingly, in this wavelength region, there are ample readily available plasmonic materials, as summarized in Fig. 9(a) and Table 3. These materials include gallium (Ga), indium (In) [215, 221], tin (Sn), bismuth (Bi) [222, 223], antimonide (Sb) [224], rubidium (Rd), magnesium (Mg) [225], rhodium (Rh) [226], ruthenium (Ru), tungsten (W), titanium (Ti), chromium (Cr), palladium (Pd), copper (Cu), platinum (Pt) [227], and semiconductors. Optical properties of alternative plasmonic materials for UV wavelengths and nanostructures on their base have been extensively studied in the last decade [228]. Fig. 9(a) shows the tendency of electric

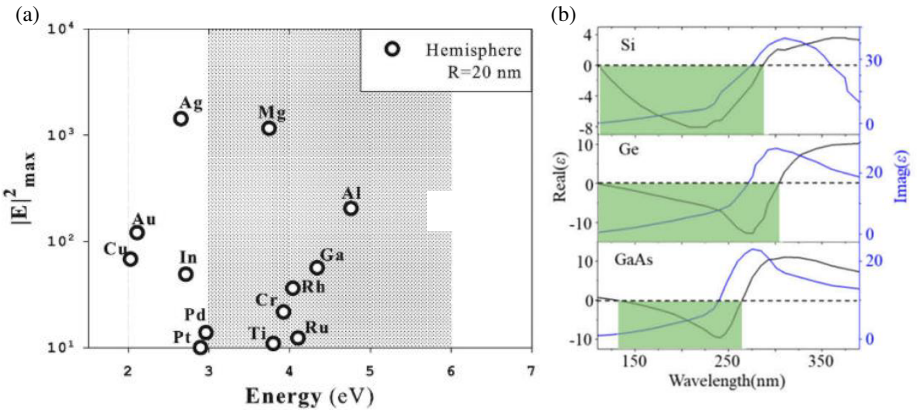

FIGURE 9. (a) Electric fields enhancement of plasmonic hemispherical particles with radius 20 nm in the UV region (grey shaded area) of 3–6 eV (400–200 nm). Reproduced with permission [226]. (b) Real and imaginary parts of permittivities of Si, Ge, and GaAs. Reproduced with permission [220].

field enhancement of hemispherical plasmonic nanoparticles with radius 20 nm in the UV region [226]. Mg nanoparticles exhibit stronger field enhancement than other materials.

Recently, Mg has been studied as an alternative plasmonic material for UV wavelengths [206, 208, 225, 229]. Among Mg advantages are its abundance, biocompatibility, and lightweight (two-thirds lighter than Al). Mg-based helical nanostructures were synthesized by the glancing angle deposition method on a quartz substrate [230] and tested for refractometric sensing with different concentrations of dimethyl sulfoxide (DMSO) in water as analyte [206]. Magnesium is prone to oxidization in air, so, the structures were coated with a 4 nm thick HfO_2 protection layer. Nanohole arrays on an Mg film were studied for the enhancement of a UV fluorescent dye [207]. A 90 nm thick Mg film with a 10 nm thick Al seed layer was deposited by sputtering. Then, arrays with 30–50 nm diameter holes were made. The UV dye (p-terphenyl) emitting at 360 nm was excited by a 266 nm femtosecond pulse. The Mg film showed 7.2 times reduction of fluorescence lifetime, as opposed to 5.3 times reduction by the Al film with the same geometry, illustrating the advantage of Mg in UV wavelength applications. Mg nanoparticles can be chemically synthesized with several different shapes, such as hexagon [229], tent, chair, and taco kite shapes [231], which give different LSP responses.

Rhodium has also been extensively studied as a plasmonic material for UV wavelengths owing to its resistance to corrosion and oxidation, contrary to Al and Mg, which oxidize with the following degradation of their plasmonic properties and enhancement factor [232]. SERS applications on the UV wavelengths were first demonstrated in rough Rh and Ru films modeled as spheroids shape islands or particles [209]. Rh spheroids (45 nm and 15 nm for long and short axis, respectively) show net $EF = 100$ at 325 nm excitation wavelength with the pyridine dye. The authors also showed that the EF for Ag is almost 0 at this wavelength due to strong dumping and small negative permittivity, while Ag's EF can be over $\sim 10^5$ around 500 nm in the visible wavelength and Rh is hardly ~ 10.

Later, Rh nanoparticles with different geometry, e.g., nanotubes and nanotripods, have been synthesized and studied for UV-SERS applications. Rh nanotripods were shown to exhibit 4.5 times Raman signal enhancement from p-aminothiophenol (PATP) analyte comparing with the Raman signal from a bare Si substrate without Rh nanotripods [210]. Rh cubes with sizes, 15, 21, and 27 nm give plasmon resonance peaks at 275 nm, 293 nm, and 313 nm, respectively. The nanocubes were fabricated by the polyol method [211]. The same polyol method was used to produce well-defined metallic nanoparticles growing in the glycol solution from seed or metal precursor [233]. $400\times$ SERS enhancement was estimated with p-aminothiophenol (PATP) molecules excited at 325 nm. The cube corners are expected to have the local electric field intensity 700 times stronger than the incidence field, which could result in $700^2 \approx 4.9 \times 10^5$ times local SERS signal enhancement. Using Rh concave nanocubes as a UV-SERS substrate, three explosives were detected [212]. The detected chemicals were p-nitrobenzoic acid (PNBA), 2,4-dinitrotoluene (DNT), and ammonium nitrate (AN) with detection limits of 10^{-10} M, 10^{-7} M, and 10^{-12} M, respectively. The enhancement factor was estimated to be 4.5×10^5 with excitation at 266 nm. Recently, Rh nanocube dimers with 32 nm cubes and 10–15 nm gaps between them were demonstrated to give 120-fold net enhancement of 350 nm autofluorescence from hemoglobin proteins excited at the 295 nm wavelength [213].

Indium nanoparticles have been studied for UV SEF and SERS applications in the last decade. For instance, Al and In dimers were theoretically studied in [234]. It showed that Al and In dimers with the optimized diameter of the dimer particles separated by a 1 nm gap give IF $= 2.0 \times 10^9$ at 208 nm and IF $= 1.2 \times 10^9$ at 359 nm. Indium core-shell nanoparticles with diameters 80 ± 20 nm were synthesized by the polyol method and coated with silica shells of 5 ± 1 and 12 ± 1 nm thicknesses for the enhancement of the UV luminescence around 360 nm [214]. Here, the silica layer functions as a spacer to avoid direct contact of the fluorophore with metal leading to the luminescence quenching. The In core-shell nanoparticles exhibited a broad plasmon resonance around

300 nm, which overlaps with the emission bands of UV-active fluorophores. Carbostyril 124 (excitation around 350 nm and emission at 420 nm) and tryptophan (excitation at 280 nm and emission at 350 nm) were chosen as model fluorophores with one of the amino acids (tyrosine and phenylalanine) responsible for the intrinsic fluorescence of proteins. Net enhancement factors of 2–3 for carbostyril 124 and 5–7 for tryptophan are observed compared with the fluorescence intensity of fluorophore on a pristine glass substrate without nanoparticles. Additionally, In nanostructures have been studied for excitation by visible light. 20 nm thick indium films support autofluorescence of proteins at 445 nm wavelength with $EF = 3.2$–7.5 [235]. In nanotriangles and nanowires excited at 632.8 nm expose SERS enhancement with $EF = \sim 1.1 \times 10^4$ and $\sim 4.9 \times 10^3$, respectively [236].

Gallium is a metal whose permittivity substantially depends on its phase [237]. For instance, solid-phase Ga can be plasmonic from $\sim$ 200–700 nm, while liquid-phase Ga can be plasmonic from $\sim$ 200 nm to the near-IR region and beyond following Drude model [238]. Ga has a low melting temperature 29.7°C and, therefore, its phase can be easily changed by temperature variations. Ga nanoparticles with various diameters ranging from 14 to 190 nm can be prepared and their localized plasmon resonances can be tuned from 233 to 717 nm [239]. Ga nanoparticles were produced by molecular beam epitaxy (MBE). They were first demonstrated in SERS applications with the visible wavelength excitation (at 633 nm) of cresyl fast violet (CFV) dye, yielding a detection range of 10–200 ppm and $EF \sim 80$ [240]. For UV light excitation, Ga nanoparticles with diameters 23, 26, and 70 nm were excited at 325 nm with crystal violet (CV) dye, giving fluorescence emission around 590 nm [216]. The 26 nm NPs have a resonance peak at 325 nm aligned with the excitation wavelength. The net SERS enhancement with $EF = 5$–22 and SEF enhancement with $EF = 2$–9 were observed, respectively. Moreover, Ga nanoparticles can work as an immunosensor for the detection of Helicobacter pylori in the refractometric sensing scheme, yielding LOD of 10×10^{-12} M [217] and 6.0×10^{-12} M [218].

Apart from the aforementioned materials, there are other miscellaneous material candidates, such as gallium platinum alloys [241], gallium-indium alloy nanoparticles [242], bismuth nanoparticles [243–245], and texturized films [223, 246] considered for their negative permittivity from the UV to near-IR wavelength ranges. Some well-known semiconductors, such as Ge, GaAs, Si can also be plasmonic for UV wavelengths from 100 to 300 nm due to the interband transitions [220], as shown in Fig. 9(b). Theoretical analysis of triangular antennas for refractometric sensing in the wavelength region of 250–300 nm, showed BRIS of 215 nm/RIU for a dimer of GaAs-based triangular nanoparticles, and only 75 and 100 nm/RIU for Si and Ge dimers, respectively. A similar study was also performed for Si dimers and air hole arrays in a Si film with BRIS of 190 nm/RIU in the wavelength range of 190–320 nm [219]. Bismuth telluride (Bi:Te) semiconductor was shown to exhibit plasmonic response in a band extending from $\sim$ 250 nm to visible or near-IR wavelength, depending on the Bi doping in the alloy composition [247]. For instance, a 134 nm thick film of Bi (34%):Te (66%) exhibits negative permittivity for the 250–660 nm band. The upper cut-off wavelength can be tuned from 530 to 978 nm by changing the composition of Bi:Te from 6% to 60% of Bi. Topological insulators, for instance, $Bi_{1.5}Sb_{0.5}Te_{1.8}Se_{1.2}$ (BSTS), are a class of materials, where the bulk is an insulator, but the surface, where electrons are sufficiently mobile, is conductive [248]. A BSTS crystal has a 1.5 nm thick plasmonic layer exhibiting negative permittivity from 200 and 670 nm, while the rest of 0.5 mm thick crystal is dielectric. Focused ion beam (FIB) milling was used to pattern 1D and 2D grating structures displaying plasmonic resonances between 350 and 550 nm. The optical properties of alternative materials for UV wavelengths have been extensively studied and these plasmonic materials have been applied for SERS and SEF. However, there are few experimental demonstrations of sensing applications of these materials.

6. DOPED SEMICONDUCTORS

Doped semiconductors as plasmonic materials have been developed for surface-enhanced mid-infrared absorption spectroscopy (SEIRA) in the last decade [249–251]. The attractive feature is the tunable plasma wavelength, adjusted in the broad mid-infrared wavelength region by different doping levels. The mid-IR range hosts absorption bands of many important analyte molecules, as illustrated in Fig. 10. The doped semiconductors include conventional group IV semiconductors [252], like silicon (Si) [253] and germanium (Ge), and compound III-V semiconductors such as gallium arsenide (GaAs) [254], indium phosphide (InP) [255], indium arsenide (InAs) [256–258], and indium antimonide (InSb) [259], as summarized in Table 4. The nanostructures from doped semiconductors were shaped in various forms, such as monopole, dipole antennas, nanoparticles, gratings, and metasurfaces. The aim is to realize high localization of fields for infrared light to enhance the absorption rates

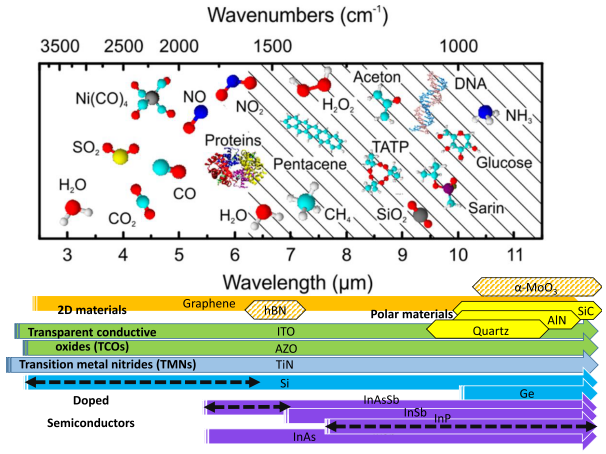

FIGURE 10. Mid-infrared absorption peaks of analyte molecules and plasmonic wavelengths ranges of doped-semiconductors, TCOs, graphene, and phononic wavelengths of polar materials for mid-infrared wavelengths. The dashed dark arrows indicate the reported tunable ranges of plasma wavelengths λ_p by doping. Note that hBN and α-MoO_3 become hyperbolic materials with at least one of the permittivity components negative and the others positive for the indicated wavelength ranges. Reproduced with permission [260].

TABLE 4. Summary of doped semiconductors, TCOs, polar materials, graphene, and 2D materials for mid-IR absorption spectroscopy. CBP: the organic semiconductor 4,4'-bis(N-carbazolyl)-1,1'-biphenyl. CEMS: chloroethyl methyl sulfide. EBL: electron beam lithography. NR: nanoribbon. LEPECVD: low-energy plasma-enhanced chemical vapor deposition. MOVPE: metal-organic vapor phase epitaxy. PL: photolithography. PTCDA: perylene-3,4,9,10-tetracarboxylic dianhydride. YSZ: yittrium stabilized zirconia. ″: same as above. *: Reststrahlen band of phononic materials. **: phonon band of combined polar materials. #: refractometric sensing. λ_p: plasma wavelength, $\lambda_p = 2\pi c/\omega_p$.

Material & structure/substrate	Plasma wavelength λ_p [μm]	Damping constant γ [THz]	Deposition/fabrication method	Analyte/LOD	Ref.
B: Si/Si	5.39–6.43	19.64–23.52	Ion implantation	–	[253]
P: Si/Si	3.79–5.54	19.33–49.22			
P: Si discs/silica-Si	∼ 2–5	17.26–56.43	″, EBL, RIE	–	[261]
Ge antennas/Si	10.26	–	LEPECVD	PDMS, CEMS	[262]
Si: InSb/GaAs	6.9	2.5	MBE	–	[259]
Si: InAs disc/GaAs	5.5	5.0	″	PMMA	[256]
Si: InAs/GaAs	5.48	7.69	″	–	[257]
Si: InAsSb antennas/GaSb	5.35	1.59	″	Vanillin	[263]
″ gratings/GaSb	″	″	″	PDMS	[264]
Si: InP/InP	7.4–22.7	2.16–2.82	MOVPE	–	[255]
ITO nanorods/YSZ	0.673	–	EBL	Streptavidin	[170]
AZO trenches/Si	2.02	35	ALD	Silica	[65]
TiN trenches/Si	∼ 0.5	49.31	PEALD	Vanillin	[110]
Graphene NR/silica-Si	–	–	CVD, EBL	IgG protein	[265]
″	–	–	″	PTCDA dye	[266]
″	–	–	″	Deoxynivalenol	[267]
Graphene NR/CaF_2	–	–	″	NO_2, N_2O, NO, SO_2 gas	[268]
#Graphene NR/silica-Si	–	1.49	″	CO_2 gas/390–2000 ppm	[269]
hBN gratings/CaF_2	6.21–7.35*	0.12–0.15	EBL	CBP	[270]
hBN flake/silica-Si	″		–	″	[271]
#hBN nanoribbons/CaF_2	″	0.45	EBL	CO_2 gas/390–10000 ppm	[272]
hBN flake/Al grating-CaF_2	″	–	EBL	CoPc	[273]
hBN, α-MoO_3/Quartz	5.88–12.5**	–	–	–	[274]
4H-SiC gratings/SiC	10.3–12.6*	0.06	PL	Cyclohexane	[275]

of analyte molecules. Initially, the nanostructures for SEIRA were made of gold [40].

In general, semiconductors for visible to mid-IR wavelengths (below the bandgaps) are dielectric materials with positive permittivities due to low concentrations of free charges. However, after high doping, the carrier concentration can be increased, and permittivity becomes negative. The latter can be accurately represented by the Drude-Lorentz model:

$$\varepsilon_m(\omega) = \varepsilon_1 + i\varepsilon_2 = \varepsilon_\infty\left(1 - \frac{\omega_p^2}{\omega^2 + i\omega\gamma}\right) + \sum_j \frac{S_j\omega_{f,j}^2}{\omega_{f,j}^2 - \omega^2 - i\omega\Gamma_j}, \quad (5)$$

where ε_∞, ω_p, and γ in the Drude term are the high-frequency dielectric constant, plasma frequency, and electrons plasma damping. The Lorentzian part of the dielectric function $\varepsilon_m(\omega)$ contains S_j, $\omega_{f,j}$, and Γ_j, which are the strength, resonance frequency and damping for the j^{th} Lorentz oscillator, respectively.

The plasma frequency is

$$\omega_p = \sqrt{\frac{n_e e^2}{m_e \varepsilon_0}}, \quad (6)$$

where n_e is the free charges concentration, e is the electron charge, m_e is the effective electron mass, and ε_0 is the permittivity of vacuum. The plasma frequency (or wavelength), as seen from Eq. (6), can be tuned by the doping level, which influences n_e. The larger n_e becomes, the larger the plasma frequency (or shorter the wavelength). The positive or negative dopants can also tune the plasma frequency by affecting the effective mass of carriers, m_e. For instance, with a positive dopant, the effective mass is larger resulting in a smaller plasma frequency.

IV-group semiconductors, Ge and Si are compatible with the current microelectronics fabrication. Hence, using Si as the main ingredient of SEIRA chips is highly advantageous for integration, scaling, and mass productivity. Silicon can be doped

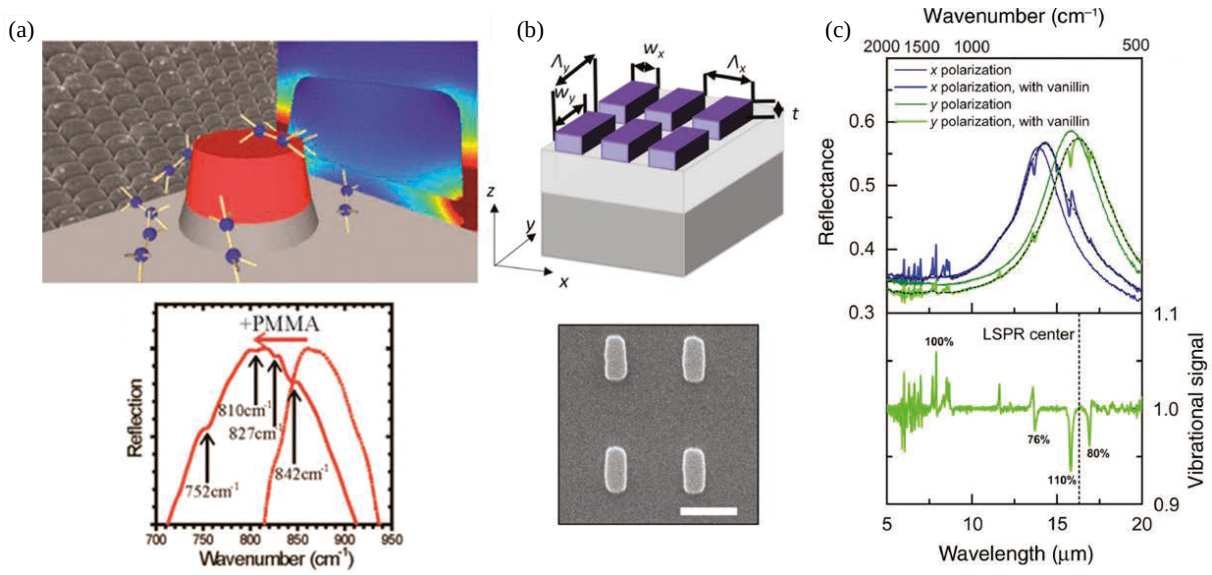

FIGURE 11. Doped semiconductors for SEIRA spectroscopy. (a) InAs discs nanoantennas and reflection spectra with and without PMMA analyte. Reproduced with permission [258]. (b) Si-doped InAsSb monopole antennas and (c) their optical response with vanillin analyte. Reproduced with permission [263].

by ion implantation of boron (B) for p-type and phosphorus (P) for n-type semiconductors, respectively [253]. The concentration of dopant is high within several hundreds of nanometers near the surface, 3×10^{20}–1×10^{21} cm^{-3}, and then is exponentially lowering. Post-annealing extends the donor concentration 1×10^{20} cm^{-3} into the Si at depths between 600 and 2000 nm. A n-type semiconductor tends to have a shorter plasma wavelength due to negative charges and smaller effective mass. The plasma wavelength varies from 5.39 to 6.43 μm and 3.73 to 5.54 μm for p-doped and n-doped Si, respectively. Highly doped Si with 10^{20}–10^{21} cm^{-3} free carrier concentration has been reported [261]. It was used for the fabrication of a nanodisc array on an SOI substrate. The nanodisc array with a disk diameter of 100 nm and thickness of 23 nm supports LSP resonances, which are tunable by the doping level between 2.5 to 5 μm.

A phosphorous-doped Ge dipole antenna array was fabricated by EBL on a Si substrate. Each dipole antenna consists of a pair of bars whose total length is approximately half of the operating wavelength [262]. Phosphorus donor pushed the doping level to $n_e \approx 2.3 \times 10^{19}$ cm^{-3}, resulting in the plasma wavelength around 10 μm. Compared with Si, Ge has the advantage of a smaller electron effective mass ($m_e \approx 0.12$ for n-type Ge and $m_e \approx 0.26$ for n-type Si), which allows higher ω_p for a given doping level and widens the wavelength range of applications of plasmonic sensing. The fabricated dipoles have a pair of 1 μm wide and 1–4 μm long Ge-doped bars with a 300 nm gap, see Fig. 11(a). The antenna was used for sensing two chemical agent molecules. A spin-coated polydimethylsiloxane (PDMS) polymer film with a vibrational signal at 12.5 μm (800 cm^{-1}) and the chloroethyl methyl sulfide (CEMS), a chemical weapon agent with a vibrational band at 14.49–13.38 μm (690–720 cm^{-1}) were detected with the vibrational signal enhancements of up to 2 orders of magnitude (~ 100) compared with the analytes on a bare substrate.

Some III-V semiconductors have large electron mobility and low carriers' effective mass, resulting in large plasma frequencies. Nevertheless, there are several cases of III-V semiconductors in SEIRA applications. Nanoparticles of n+(Si) doped InAs were studied in [258]. The InAs discs are 400 nm in diameter and 200 nm in height. They were arranged in a lattice with a 550 nm period on a 1.3 μm thick undoped InAs layer on GaAs substrate, as shown in Fig. 11(b), and support a LSP resonance around 10 μm. Fabrication was done by nanosphere lithography, where an array of spheres is used as a mask. A 50 nm thick PMMA layer was spin-coated as an analyte, giving multiple vibrational signals at 752 cm^{-1} (C-C stretch), 827 cm^{-1} (C-O-C stretch), and 842 cm^{-1} (CH_2 rocking).

InAsSb-based nanostructures were developed for molecular sensing [264]. The InAsSb film (100 nm thick) was grown by molecular beam epitaxy (MBE) on a GaSb substrate with a 500 nm thick GaSb buffer layer to match the lattices of the substrate and the InAsSb film. It was doped with Si with the levels of 6.6×10^{19} cm^{-3}, 4.0×10^{19} cm^{-3}, and 2.2×10^{19} cm^{-3}. The nanostructures are one-dimensional line gratings patterned by photolithography and wet etching on the GaSb buffer layer over the substrate. These gratings have 2 μm pitch and width of 265, 465, 490 nm, giving a broad resonance around 13 μm (780 cm^{-1}). A 15 nm-thick layer of polydimethylsiloxane (PDMS) polymer was spin-coated and used as a model analyte with the signal of Si-C stretching bonding at 12.5 μm (800 cm^{-1}). Si-doped InAsSb nano-antennas exhibited vibrational signal enhancement by two orders of magnitude. The InAsSb-based monopole antenna arrays was realized for chemical sensing [263] (Fig. 11(b)). Si-doped $InAs_{0.91}Sb_{0.09}$ films were lattice-matched grown on a 200-nm-thick GaSb buffer layer on top of the GaSb substrate. The doping level of the

InAsSb film was 5.1×10^{19} cm^{-3} corresponding to the plasma wavelength $\lambda_p = 5.35\mu$m. Resonators with side lengths $w_x = 540 \pm 30$ nm, $w_y = 600 \pm 40$ nm and thickness $t = 100$ nm were patterned by EBL with period $\Lambda = 1.4$ µm. Such InAsSb nano-antennas possess a resonance at 14–16 µm with the field enhancement factor of 10^3 to 10^4 at the hot spot of the antenna compared with the electric field of incident light. Vanillin as an analyte exhibits three vibrational signals with the resonance at 13.65, 15.81, and 16.95 µm (732, 632, and 590 cm^{-1}, Fig. 11(c)). The enhancement factor of 5.7 times compared with the unstructured doped InAsSb film was reported.

Apart from doped semiconductors, polar materials whose permittivity becomes negative for certain wavelength intervals in the mid-IR region due to phonon resonances in the lattice, often referred to as Reststrahlen band [276], have been challenged for mid-IR sensing. The permittivity of polar materials for mid-IR wavelength takes the form of

$$\epsilon(\omega) = \epsilon_\infty \left(1 + \frac{\omega_{LO}^2 - \omega_{TO}^2}{\omega_{TO}^2 - \omega^2 - i\omega\gamma}\right), \quad (7)$$

where ϵ_∞ is the high-frequency permittivity, ω_{LO} and ω_{TO} are transverse optical (TO) and longitudinal (LO) phonon frequencies, and γ is the scattering rate. For instance, silicon carbide (SiC) has the Reststrahlen band with negative permittivity for 10.3–12.6 µm (972–792 cm^{-1}) with parameters $\epsilon_\infty = 6.56$, $\omega_{LO} = 973$ cm^{-1}, $\omega_{TO} = 797$ cm^{-1}, and $\gamma = 4.76$ cm^{-1} in Eq. (7) [277]. SiC one-dimensional gratings with period $\Lambda = 5$–10 µm and height $H = 0.8$–24.8 µm were used for molecular sensing [275]. The SiC gratings form a cavity between the top and the bottom, where a guided phonon mode within the Reststrahlen band is trapped. Cyclohexane has an absorption band (CH_2 rocking) at 11.0 µm (903 cm^{-1}) in the center of the Reststrahlen region. As a result, the vibrational signal of the analyte strongly couples with the cavity mode within the gratings. In this strong coupling regime, the vibrational signal splits and shifts in wavelength with the increasing concentration of cyclohexane. This effect was utilized for refractometric sensing. Different liquid analytes, acetone, isopropanol, toluene, and cyclohexane were characterized in the sensing mode, yielding bulk refractive index sensitivities $S_B = 118$ cm^{-1}/RIU for TM and $S_B = 125$ cm^{-1}/RIU for TE polarizations, respectively.

Other polar materials, such as aluminum nitride (AlN) [278, 279] and quartz [280], also exhibit the Reststrahlen band at 11.5–15.0 µm (870–668 cm^{-1}) and might be tested for sensing purposes. In difference with the plasmonic behavior of SiC or AlN limited to the Reststrahlen band, vanadium oxide (VO_2) is a natural hyperbolic material with $\varepsilon_o < 0$ and $\varepsilon_e > 0$ for the mid-IR region $\sim$ 13.5–16.5 µm (740–606 cm^{-1}). Being a phase change material, VO_2 supports hyperbolicity only for temperatures below 68°C [281].

7. TWO-DIMENSIONAL MATERIALS FOR MID-INFRARED WAVELENGTHS

Recently, we have witnessed the growing interest in very "thin" materials with thicknesses from a monoatomic layer to tens of nanometers. All these materials are grouped under the title "2D materials". In general, 2D materials embrace unique electronic and optical properties, substantially different from those of bulk materials. The main reason is the strong and mostly two-dimensional confinement of electrons within ultra thin films [24–28]. There is a wide variety of 2D materials with different compositions of chemical elements. Some 2D materials consist of a single element, for example, graphene is with carbon (C), black phosphorene is with phosphorus (P), and silicene is with silicon (Si). Others are composed of multiple elements. For instance, hexagonal boron nitride (hBN) is composed of two elements. MXenes have an even more complicated constitution being composed of atomic layers of transition metal carbides, nitrides, or carbonitrides. Recently, transition metal dichalcogenide (TMD) monolayers have been synthesized as new materials. TMDs are expressed by a generalized formula of MX_2 where M is a transition metal (Mo, W, Ta, etc.) and X is a chalcogen (S, Se, or Te). Notably, they are naturally anisotropic due to their van der Waals nature. Below the exciton absorption band in a broad spectral region for near-IR wavelengths, some TMD materials exhibit very low optical loss [282]. Several TMD flakes with 50–400 nm thickness, such as tellurium disulfide (TeS_2), tellurium selenide ($TeSe_2$), and niobium diselenide ($NbSe_2$) are plasmonic and even natural hyperbolic 2D materials, with at least one of the permittivity components taking a negative value while others being positive for near-IR wavelengths [282]. For mid- to far-infrared wavelengths, hafnium disulfide HfS_2 and hafnium diselenide $HfSe_2$ become hyperbolic materials [283]. Although there are some studies of TMDs-based optical biochemical sensing [284], transition metal dichalcogenide applications in optical sensing schemes are still scarce. In difference, TMDs [282] have been extensively studied for biosensing applications with electrical read-out [285, 286].

Graphene is a monolayer carbon sheet and is probably the thinnest known plasmonic material. The permittivity of graphene becomes negative for mid-infrared wavelengths beyond $\sim$ 2 µm and down to THz frequencies and hence used for various relevant applications [52, 287–289]. Graphene as a plasmonic material supports short-range SPPs (SR-SPPs). The latter contrary to well-known long-ranged SPPs, have higher localization properties, and the thinner the plasmonic layer, the more SR-SPP is localized [290]. Highly localized plasmon modes have been observed for mid-IR wavelengths around 9.7–11.06 µm (cm^{-1}) with effective plasmon wavelength 1/40 of light wavelength in vacuum [291].

An array of graphene nanoribbons under voltaic tunability was demonstrated for protein detection [265]. The graphene nanostructures were fabricated by EBL on top of a silica layer on the Si substrate with gold electrodes, as shown in Figs. 12(a), (b). A graphene nanoribbon enables electric field localization more tightly than conventional Au nanoantennas (Figs. 12(c), (d)). Graphene's conductivity (and consequently permittivity) can be tuned by chemical potential via electrical gating in the spectral range from 5.5 to 7.7 µm (1800 to 1300 cm^{-1}), as shown in Fig. 12(e), to shift its plasmon resonance to overlap with the vibrational signal of the analyte. Such tuning by free carriers injection can be realized either through electrical gating

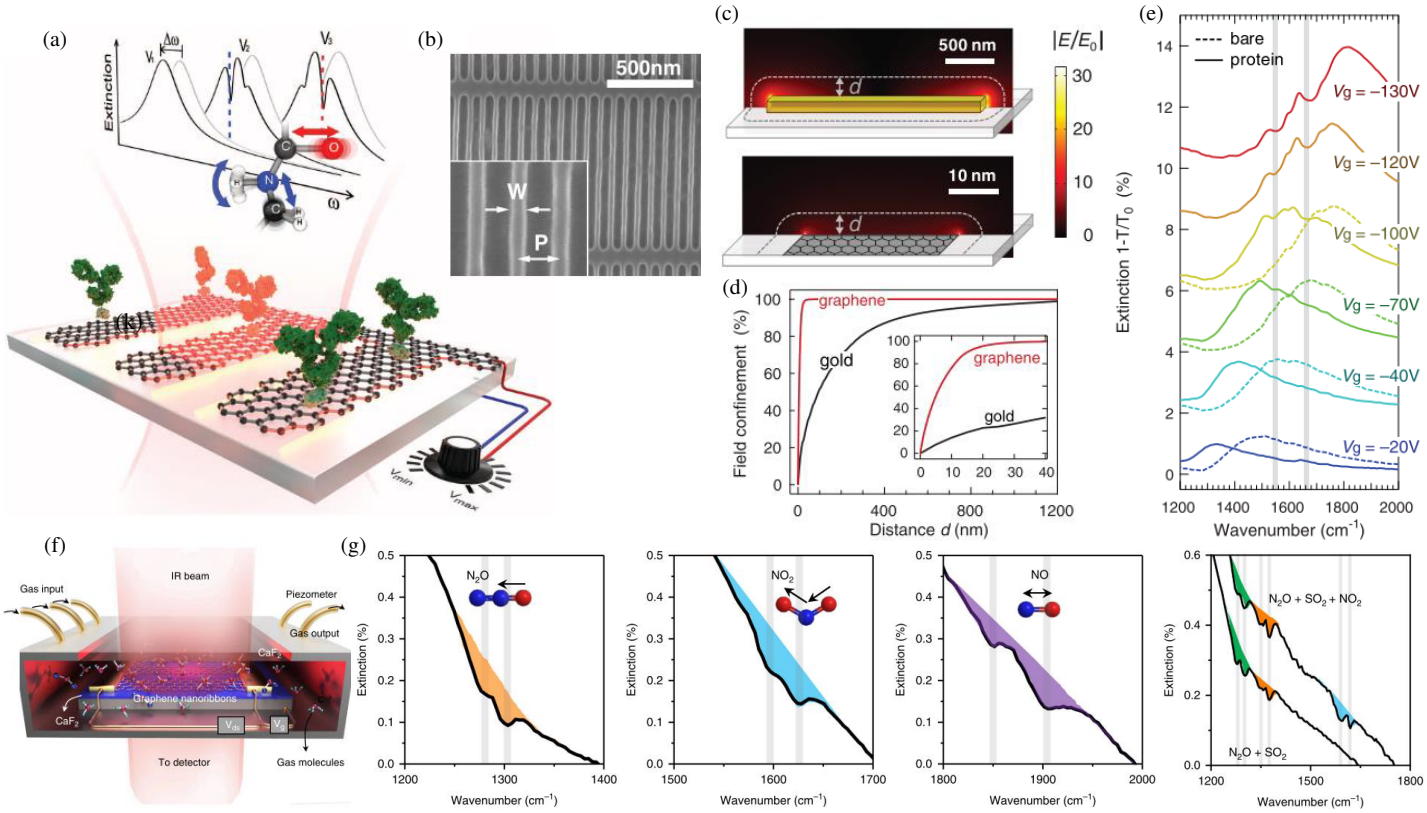

FIGURE 12. Graphene metasurfaces for SEIRA applications. (a) Conceptual view of the graphene biosensor where the plasmonic resonance is electrostatically swept continuously over the protein vibrational bands. (b) Scanning electron microscope (SEM) image of a graphene nanoribbon array in top-view. (c), (d) Electric field profile of Au (above) and graphene (below) nanoantenna at 1600 cm^1 of resonance frequency. (e) Extinction spectra (vibrational signal) of the graphene nanoribbon array for bias voltages V_g from -20 V to -130 V before (dashed curves) and after (solid curves) protein bilayer formation. Gray vertical strips indicate amide I and II vibrational bands of the protein. Reproduced with permission [265]. (f) Conceptual illustration of graphene gas sensor. (g) Extinction spectra of various gas species. Reproduced with permission [268].

(as exemplified above) or by chemical doping with great ease due to its two-dimensional nature. Chemical doping or electrical gating can increase the free carriers concentrations to the levels of 1×10^{-12}–1×10^{-13} cm^{-2} [288]. The surface is further biofunctionalized for detecting immunoglobulin G (IgG) protein. Vibration signals of the amide-I at 6.0 μm (1660 cm^{-1}) and amide-II at 6.5 μm (1537 cm^{-1}) were observed in the transmission spectra, which are the signature of binding between protein, IgG, and an antibody.

In a similar arrangement of graphene nanoribbons with 90–150 nm width on a 280 nm thick SiO_2 layer on top of the Si substrate, a 16 nm-thick layer of organic dye perylene-3,4,9,10-tetracarboxylic dianhydride (PTCDA) was detected [266]. Here, graphene plasmon modes are spectrally positioned to overlap with both C-C ring breathing modes around 6.3 μm (1590 cm^{-1}) and C=O stretching modes around 5.8 μm (1730 cm^{-1}) of the analyte. The detection of mycotoxin called deoxynivalenol, which has vibrational signals of C-O-H bending at 7.09 μm (1410 cm^{-1}), 7.01 μm (1425 cm^{-1}) and CH_3 bending at 6.93 μm (1442 cm^{-1}) was demonstrated by a graphene system of nanoribbons with period 200 nm and width 80 nm under the voltage tunability [267].

Graphene nanoribbons with 100 nm width on CaF_2 substrate were used for gas sensing [268, 269]. In this study as shown in Figs. 12(f), (g), four different gas species were analyzed in the wavelength region of $\sim$ 5.3–7.7 μm ($\sim$ 1300–1900 cm^{-1}), namely, NO_2 (1590 and 1610 cm^{-1}), N_2O (1280 and 1305 cm^{-1}), NO (1838 and 1906 cm^{-1}), and SO_2 (vibrational signals at 1347 and 1374 cm^{-1}). Since the vibrational signals of the gases are quite separated, each gas can be distinguished even from the gas mixture. Here electrical gating was also used and 30 V was applied to tune the graphene plasmon to yield the maximum gas vibrational absorption signals. Most of graphene plasmon's energy is localized within the 5 nm distance from the graphene ribbons, which gives an extremely high concentration of electric fields in the region comparable to the size of molecules. Thus, graphene plasmons boost the vibrational signals of gas molecules. CO_2 gas detection was also demonstrated by graphene nanoribbons with a period of 90 nm and width of 50 nm on the 285 nm thick SiO_2 layer on silicon. The bias voltage of 100 V was applied [269]. The structure is covered by 10 nm thick ultrathin polyethylenimine (PEI) polymer. Here, the role of the PEI polymer is to absorb CO_2 gas molecules and immobilize them within the polymer film. The refractometric sensing scheme in this case is based on changes

in the refractive index of the PEI layer as it absorbs CO_2 gas molecules. As a consequence of absorption, the localized plasmon resonance shifts from 1350 to 1400 cm^{-1}. The optical response reverses when the CO_2 concentration is lowered, and the PEI layer desorbs CO_2. The CO_2 detection range of 390–2000 ppm was demonstrated.

Hexagonal boron nitride (hBN) is an uniaxial birefringent 2D material with the optical axis normal to the surface. It exhibits hyperbolic dispersion for two wavelength ranges: type-II hyperbolic materials $\varepsilon_o < 0$, $\varepsilon_e > 0$ [292] for 6.21–7.35 µm (1360–1610 cm^{-1}) and type-I hyperbolic materials $\varepsilon_o > 0$, $\varepsilon_e < 0$ for 12.2–13.4 µm (746–819 cm^{-1}), which lies within the Reststrahlen bands [276, 293]. The ordinary and extraordinary permittivity components can be characterized by expression [270]

$$\epsilon_{o,e}(\omega) = \epsilon_{o,e\infty}\left(1 + \frac{\omega_{o,eLO}^2 - \omega_{o,eTO}^2}{\omega_{o,eTO}^2 - \omega^2 - i\omega\gamma_{o,e}}\right), \quad (8)$$

where $\epsilon_{o\infty} = \epsilon_{e\infty} = 4.52$, $\omega_{oLO} = 746\,cm^{-1}$, $\omega_{eLO} = 819\,cm^{-1}$, $\omega_{oTO} = 1360\,cm^{-1}$, $\omega_{eTO} = 1610\,cm^{-1}$, $\gamma_o = 4\,cm^{-1}$, $\gamma_e = 5\,cm^{-1}$. In numerical analysis and modeling of SEIRA nanostructures, the permittivity of analyte molecules for mid-IR wavelengths is often approximated by the Lorentz oscillator model in a similar form. Example analytes are proteins [294], gas molecules [268], cyclohexane and acetone [275], 4,4'-bis(N-carbazolyl)-1,1'-biphenyl (CBP) [270], and silica [295]. Within the hyperbolic regions of hBN highly localized phonon-polariton modes can propagate with a much shorter effective wavelength than in vacuum. An array of hBN nanoribbons in the type-II hyperbolic region support cavity modes used for the molecular detection in [270]. hBN nanoribbons were fabricated by EBL on the CaF_2 substrate with a period of 400 nm, width of 85–162 nm, and thickness of 43 nm. As estimated, over 85% of the electric field is concentrated within the 30 nm distance from the nanoribbon surface. A model analyte was an organic semiconductor CBP deposited on the hBN surface with thicknesses 1–20 nm. Strong coupling between the phonon resonance mode of hBN nanorribons and the absorption resonance of the CBP layer associated with C-H vibration at 6.9 µm (1450 cm^{-1}) occurs. The correlated splitting of the transmitted modes was observed for the thickness of the analyte layer larger than 3 nm (see Fig. 13(a)).

Unpatterned hBN sheets placed on top of the analyte layer were demonstrated for molecular sensing in the strong coupling regime [271]. The structure composed of 85 nm thick hBN flakes is placed on top of a 100 nm thick CBP analyte layer deposited on a 150 nm thick silica layer and Si substrate. Hyperbolic phonon-polariton modes in the hBN sheet interact with the analyte layer underneath and exhibit mode splitting of the vibrational signal of the CBP layer and resonance of hBN phonon-polaritons around 6.8 µm (1450–1460) cm^{-1}, which is a signature of strong coupling.

Coupling between vibrational modes of analyte molecules and modes of the 2D material structures was demonstrated for two different wavelength regions [273]. The structure under consideration consists of 75 nm thick hBN flakes and 50 nm thick Al gratings on CaF_2 sandwiching an 80 nm thick cobalt(II) phthalocyanine (CoPc) layer, as illustrated in Fig. 13(b). CoPc molecules support both a vibrational resonance in mid-IR at 6.55 µm (1525 cm^{-1}) and two excitonic resonances in visible with wavelengths 694 and 617 nm (14400 and 16200 cm^{-1}). There are two types of coupling in such a system. The phonon modes in the hBN flake and vibrational signals of the CoPc layer are coupled in the structure at mid-IR wavelengths. Coupling between Al gratings surface plasmon-polaritons and CoPC molecules excitonic resonances occur at visible wavelengths. Hybridized phonon-polaritons and plasmon modes in the structures were used to enhance vibrational and excitonic signals of the CoPc layer, and mode splitting in the strong coupling regime for both wavelength regions was observed.

CO_2 gas was detected by 30 nm thick hBN nanoribbons with 400 nm period on the wavelengths around 6.80 µm (1470 cm^{-1}) [272]. The sensing structure is covered by a 75 nm thick PEI film that absorbs CO_2 molecules. Similar to the case of CO_2 detection by graphene nanoribbons with the PEI layer, the detection principle here is based on refractometric sensing when increasing CO_2 concentration results in the resonance shift from 6.76 to 6.78 µm (1478 to 1476 cm^{-1}) for the concentration changes between 390 and 10000 ppm.

Although these materials are natural hyperbolic materials, their bandwidths are limited to certain wavelengths. To cover an expanded mid-IR range 5.88–12.5 µm (1700–800 cm^{-1}) it was proposed to exploit few 2D materials with different optical phonon bands together [274]. In this example, materials are hBN and α-MoO_3 flakes on a polar quartz substrate. Phonon-polariton modes from each 2D material layer and the polar substrate hybridize creating different phonon modes. Hybridization of surface plasmons on the graphene layer and phonon-polariton modes in the hBN layer enabling modification of each of the modes has also been reported [293].

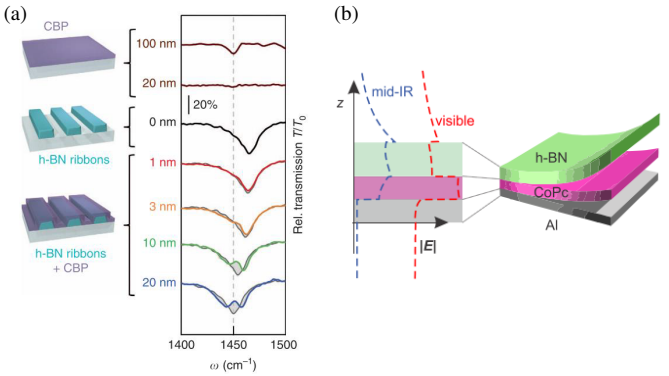

FIGURE 13. Hexagonal boron nitride (hBN) for SEIRA. (a) Experimental infrared transmission spectra of hBN ribbon arrays with different CBP coating. The hBN ribbon array with 20 × 20 μm^2 size, period 400 nm, and ribbon width 158 nm. Reproduced with permission [270]. (b) Schematic of the three-layer structure (50 nm Al/50 nm CoPc/75 nm hBN) for Dual-band polaritons and molecular excitations at both visible and mid-IR frequencies. Left panel: blue and red dashed lines show the mode profile of the polaritonic modes in the mid-IR and visible frequency ranges, respectively (blue line for 1530 cm^{-1}, red line for 19500 cm^{-1}). Reproduced with permission [273].

8. SUMMARY

We provide an overview of the recent development of novel plasmonic materials, other than conventional gold, silver, copper, and aluminum, used in biochemical sensing applications. Sensing examples cover vast wavelength regions from UV to mid-IR with different optical sensing schemes. Each wavelength region has its peculiar sensing schemes and sensitivity enhancement mechanisms. For UV wavelengths, mainly circular dichroism spectroscopy and autofluorescence are used. The visible to near-IR regions host the most widely used sensing techniques, such as refractometric, fluorescence label, and Raman-based sensing. The mid-IR wavelength region is for vibrational absorption spectroscopy. For each sensing scheme requirements for plasmonic materials are different. For instance, in the case of localized surface plasmon resonance supported on nanoparticles, negative permittivity around -2 is most wanted for the wavelength region of interest, and thus tunability of permittivity is indispensable. Therefore, a broad nomenclature of appropriate plasmonic materials is highly desirable. At the same time, a growing number of new 2D materials have been discovered and studied recently, some of which give unique plasmonic and hyperbolic properties in various wavelength regions from visible to mid-IR. These emerging materials may be further exploited in sensing, as some of them possess favorable optical and plasmonic properties for this purpose.

ACKNOWLEDGEMENT

This work was supported by Independent Research Fund Denmark, DFF Research Project 2 "PhotoHub" (8022-00387B). The authors would like to acknowledge the support from the Danish National Center for Micro- and Nanofabrication (DTU Nanolab).

REFERENCES

[1] Maier, S. A. and H. A. Atwater, "Plasmonics: Localization and guiding of electromagnetic energy in metal/dielectric structures," *Journal of Applied Physics*, Vol. 98, 1–10, 2005.

[2] Maier, S. A., *Plasmonics: Fundamentals and Applications*, Springer, New York, NY, 2007.

[3] Barnes, W. L., A. Dereux, and T. W. Ebbesen, "Surface plasmon subwavelength optics," *Nature*, Vol. 424, No. 6950, 824–830, 2003.

[4] Sandtke, M. and L. Kuipers, "Slow guided surface plasmons at telecom frequencies," *Nature Photonics*, Vol. 1, No. 10, 573–576, 2007.

[5] Aubry, A., D. Y. Lei, A. I. Fernández-Domínguez, Y. Sonnefraud, S. A. Maier, and J. B. Pendry, "Plasmonic light-harvesting devices over the whole visible spectrum," *Nano Letters*, Vol. 10, No. 7, 2574–2579, 2010.

[6] Wang, P., A. V. Krasavin, L. Liu, Y. Jiang, Z. Li, X. Guo, L. Tong, and A. V. Zayats, "Molecular plasmonics with metamaterials," *Chemical Reviews*, Vol. 122, No. 19, 15 031–15 081, 2022.

[7] Yang, Y., J. Seong, M. Choi, J. Park, G. Kim, H. Kim, J. Jeong, C. Jung, J. Kim, G. Jeon, *et al.*, "Integrated metasurfaces for re-envisioning a near-future disruptive optical platform," *Light: Science & Applications*, Vol. 12, No. 1, 152, 2023.

[8] Shelby, R. A., D. R. Smith, and S. Schultz, "Experimental verification of a negative index of refraction," *Science*, Vol. 292, No. 5514, 77–79, 2001.

[9] Yao, J., Z. Liu, Y. Liu, Y. Wang, C. Sun, G. Bartal, A. M. Stacy, and X. Zhang, "Optical negative refraction in bulk metamaterials of nanowires," *Science*, Vol. 321, No. 5891, 930, 2008.

[10] Cai, W., U. K. Chettiar, A. V. Kildishev, and V. M. Shalaev, "Optical cloaking with metamaterials," *Nature Photonics*, Vol. 1, No. 4, 224–227, 2007.

[11] Ergin, T., N. Stenger, P. Brenner, J. B. Pendry, and M. Wegener, "Three-dimensional invisibility cloak at optical wavelengths," *Science*, Vol. 328, No. 5976, 337–339, 2010.

[12] Deng, Y., H. Li, and H. Liu, "On spectral properties of Neuman-Poincaré operator and plasmonic resonances in 3D elastostatics," *Journal of Spectral Theory*, Vol. 9, No. 3, 767–789, 2019.

[13] Li, H., J. Li, and H. Liu, "On novel elastic structures inducing polariton resonances with finite frequencies and cloaking due to anomalous localized resonances," *Journal des Mathématiques Pures et Appliquées*, Vol. 120, 195–219, 2018.

[14] Li, H., J. Li, and H. Liu, "On quasi-static cloaking due to anomalous localized resonance in R3," *SIAM Journal on Applied Mathematics*, Vol. 75, No. 3, 1245–1260, 2015.

[15] Han, X., K. Liu, and C. Sun, "Plasmonics for biosensing," *Materials*, Vol. 12, No. 9, 1411, 2019.

[16] Wang, C., S. Huang, Q. Xing, Y. Xie, C. Song, F. Wang, and H. Yan, "Van der Waals thin films of WTe2 for natural hyperbolic plasmonic surfaces," *Nature Communications*, Vol. 11, No. 1, 1158, 2020.

[17] Nguyen, H. H., J. Park, S. Kang, and M. Kim, "Surface plasmon resonance: A versatile technique for biosensor applications," *Sensors*, Vol. 15, No. 5, 10 481–10 510, 2015.

[18] Špačková, B., P. Wrobel, M. Bocková, and J. Homola, "Optical biosensors based on plasmonic nanostructures: A review," *Proceedings of the IEEE*, Vol. 104, No. 12, 2380–2408, 2016.

[19] Wang, Z., J. Chen, S. A. Khan, F. Li, J. Shen, Q. Duan, X. Liu, and J. Zhu, "Plasmonic metasurfaces for medical diagnosis applications: A review," *Sensors*, Vol. 22, No. 1, 133, 2022.

[20] Altug, H., S.-H. Oh, S. A. Maier, and J. Homola, "Advances and applications of nanophotonic biosensors," *Nature Nanotechnology*, Vol. 17, No. 1, 5–16, 2022.

[21] West, P. R., S. Ishii, G. V. Naik, N. K. Emani, V. M. Shalaev, and A. Boltasseva, "Searching for better plasmonic materials," *Laser & Photonics Reviews*, Vol. 4, No. 6, 795–808, 2010.

[22] Naik, G. V., V. M. Shalaev, and A. Boltasseva, "Alternative plasmonic materials: Beyond gold and silver," *Advanced Materials*, Vol. 25, No. 24, 3264–3294, 2013.

[23] Guler, U., V. M. Shalaev, and A. Boltasseva, "Nanoparticle plasmonics: Going practical with transition metal nitrides," *Materials Today*, Vol. 18, No. 4, 227–237, 2015.

[24] Low, T., A. Chaves, J. D. Caldwell, A. Kumar, N. X. Fang, P. Avouris, T. F. Heinz, F. Guinea, L. Martin-Moreno, and F. Koppens, "Polaritons in layered two-dimensional materials," *Nature Materials*, Vol. 16, No. 2, 182–194, 2016.

[25] Cai, Z., Y. Xu, C. Wang, and Y. Liu, "Polariton photonics using structured metals and 2D materials," *Advanced Optical Materials*, Vol. 8, No. 5, 1901090, 2019.

[26] Elbanna, A., H. Jiang, Q. Fu, J.-F. Zhu, Y. Liu, M. Zhao, D. Liu, S. Lai, X. W. Chua, J. Pan, *et al.*, "2D material infrared photonics and plasmonics," *ACS Nano*, Vol. 17, No. 5, 4134–4179, 2023.

[27] Lin, H., Z. Zhang, H. Zhang, K.-T. Lin, X. Wen, Y. Liang, Y. Fu, A. K. T. Lau, T. Ma, C.-W. Qiu, and B. Jia, "Engineering van der Waals materials for advanced metaphotonics," *Chemi-*

cal Reviews, Vol. 122, No. 19, 15 204–15 355, 2022.

[28] Wang, H., A. Kumar, S. Dai, X. Lin, Z. Jacob, S.-H. Oh, V. Menon, E. Narimanov, Y. D. Kim, J.-P. Wang, *et al.*, "Planar hyperbolic polaritons in 2D van der Waals materials," *Nature Communications*, Vol. 15, No. 1, 69, 2024.

[29] Gavela, A. F., D. G. Garcia, J. C. Ramirez, and L. M. Lechuga, "Last advances in silicon-based optical biosensors," *Sensors*, Vol. 16, No. 3, 285, 2016.

[30] Caldarola, M., P. Albella, E. Cortés, M. Rahmani, T. Roschuk, G. Grinblat, R. F. Oulton, A. V. Bragas, and S. A. Maier, "Non-plasmonic nanoantennas for surface enhanced spectroscopies with ultra-low heat conversion," *Nature Communications*, Vol. 6, No. 1, 7915, 2015.

[31] Finco, G., M. Z. Bideskan, L. Vertchenko, L. Y. Beliaev, R. Malureanu, L. R. Lindvold, O. Takayama, P. E. Andersen, and A. V. Lavrinenko, "Guided-mode resonance on pedestal and half-buried high-contrast gratings for biosensing applications," *Nanophotonics*, Vol. 10, No. 17, 4289–4296, 2021.

[32] Beliaev, L. Y., P. G. Stounbjerg, G. Finco, A.-I. Bunea, R. Malureanu, L. R. Lindvold, O. Takayama, P. E. Andersen, and A. V. Lavrinenko, "Pedestal high-contrast gratings for biosensing," *Nanomaterials*, Vol. 12, No. 10, 1748, 2022.

[33] Beliaev, L. Y., S. Kim, B. F. S. Nielsen, M. V. Evensen, A.-I. Bunea, R. Malureanu, L. R. Lindvold, O. Takayama, P. E. Andersen, and A. V. Lavrinenko, "Optical biosensors based on nanostructured silicon high-contrast gratings for myoglobin detection," *ACS Applied Nano Materials*, Vol. 6, No. 13, 12 364–12 371, 2023.

[34] Beliaev, L. Y., P. G. Stounbjerg, G. Finco, A.-I. Bunea, R. Malureanu, L. R. Lindvold, O. Takayama, P. E. Andersen, and A. V. Lavrinenko, "Photonic crystals based on silicon nanoholes array for biosensing applications," in *2022 Sixteenth International Congress on Artificial Materials for Novel Wave Phenomena (Metamaterials)*, X061–X063, Siena, Italy, 2022.

[35] Beliaev, L. Y., O. Takayama, and S. Xiao, "Effectively detecting cardiac myoglobin by use of bound states in the continuum in silicon nitride gratings," *Journal of Applied Physics*, Vol. 135, No. 22, 223101, 2024.

[36] Beliaev, L., O. Takayama, and A. Laurynenka, "Subwavelength periodic dielectric nanostructures for biochemical sensing," in *Biophotonics and Biosensing: From Fundamental Research to Clinical Trials Through Advances of Signal and Image Processing*, A. Armani, T. Chalyan, and D. D. Sampson, eds., 1st Edition, Chapter 5, 157-187, Elsevier, Amsterdam, 2024.

[37] Leonardi, A. A., M. J. L. Faro, and A. Irrera, "Biosensing platforms based on silicon nanostructures: A critical review," *Analytica Chimica Acta*, Vol. 1160, 338393, 2021.

[38] Homola, J., S. S. Yee, and G. Gauglitz, "Surface plasmon resonance sensors: Review," *Sensors and Actuators B: Chemical*, Vol. 54, 3–15, 1999.

[39] Anker, J. N., W. P. Hall, O. Lyandres, N. C. Shah, J. Zhao, and R. P. V. Duyne, "Biosensing with plasmonic nanosensors," *Nature Materials*, Vol. 7, No. 6, 442–453, 2008.

[40] Adato, R., S. Aksu, and H. Altug, "Engineering mid-infrared nanoantennas for surface enhanced infrared absorption spectroscopy," *Materials Today*, Vol. 18, No. 8, 436–446, 2015.

[41] Tang, L. and J. Li, "Plasmon-based colorimetric nanosensors for ultrasensitive molecular diagnostics," *ACS Sensors*, Vol. 2, No. 7, 857–875, 2017.

[42] Kakkanattu, A., N. Eerqing, S. Ghamari, and F. Vollmer, "Review of optical sensing and manipulation of chiral molecules and nanostructures with the focus on plasmonic enhancements," *Optics Express*, Vol. 29, No. 8, 12 543–12 579, 2021.

[43] Shrestha, K., S. Kim, J. Han, G. M. Florez, H. Truong, T. Hoang, S. Parajuli, *et al.*, "Mobile efficient diagnostics of infectious diseases via on-chip RT-qPCR: MEDIC-PCR," *Advanced Science*, Vol. 10, No. 28, 2302072, 2023.

[44] Cunningham, B. T., M. Zhang, Y. Zhuo, L. Kwon, and C. Race, "Recent advances in biosensing with photonic crystal surfaces: A review," *IEEE Sensors Journal*, Vol. 16, No. 10, 3349–3366, 2016.

[45] Pitruzzello, G. and T. F. Krauss, "Photonic crystal resonances for sensing and imaging," *Journal of Optics*, Vol. 20, No. 7, 073004, 2018.

[46] Quaranta, G., G. Basset, O. J. F. Martin, and B. Gallinet, "Recent advances in resonant waveguide gratings," *Laser & Photonics Reviews*, Vol. 12, No. 9, 1800017, 2018.

[47] Drayton, A., I. Barth, and T. F. Krauss, "Guided mode resonances and photonic crystals for biosensing and imaging," in *Semiconductors and Semimetals*, Vol. 100, 115–148, Elsevier, 2019.

[48] Tseng, M. L., Y. Jahani, A. Leitis, and H. Altug, "Dielectric metasurfaces enabling advanced optical biosensors," *ACS Photonics*, Vol. 8, No. 1, 47–60, 2021.

[49] Xiong, Y., S. Shepherd, J. Tibbs, A. Bacon, W. Liu, L. D. Akin, T. Ayupova, S. Bhaskar, and B. T. Cunningham, "Photonic crystal enhanced fluorescence: A review on design strategies and applications," *Micromachines*, Vol. 14, No. 3, 668, 2023.

[50] Babicheva, V. E., A. Boltasseva, and A. V. Lavrinenko, "Transparent conducting oxides for electro-optical plasmonic modulators," *Nanophotonics*, Vol. 4, No. 2, 165–185, 2015.

[51] Zhao, Y. and Y. Zhu, "Graphene-based hybrid films for plasmonic sensing," *Nanoscale*, Vol. 7, No. 35, 14 561–14 576, 2015.

[52] Huang, S., C. Song, G. Zhang, and H. Yan, "Graphene plasmonics: Physics and potential applications," *Nanophotonics*, Vol. 6, No. 6, 1191–1204, 2017.

[53] Ogawa, S., S. Fukushima, and M. Shimatani, "Graphene plasmonics in sensor applications: A review," *Sensors*, Vol. 20, No. 12, 3563, 2020.

[54] Zhou, J., T. Yang, J. Chen, C. Wang, H. Zhang, and Y. Shao, "Two-dimensional nanomaterial-based plasmonic sensing applications: Advances and challenges," *Coordination Chemistry Reviews*, Vol. 410, 213218, 2020.

[55] Hanham, S. M. and S. A. Maier, "Terahertz plasmonic surfaces for sensing," in *Active Plasmonics and Tuneable Plasmonic Metamaterials*, Chapter 8, 243-260, Wiley, 2013.

[56] Borisov, S. M. and O. S. Wolfbeis, "Optical biosensors," *Chemical Reviews*, Vol. 108, No. 2, 423–461, 2008.

[57] Ng, S. M., M. Koneswaran, and R. Narayanaswamy, "A review on fluorescent inorganic nanoparticles for optical sensing applications," *RSC Advances*, Vol. 6, No. 26, 21 624–21 661, 2016.

[58] Medintz, I. L., H. T. Uyeda, E. R. Goldman, and H. Mattoussi, "Quantum dot bioconjugates for imaging, labelling and sensing," *Nature Materials*, Vol. 4, No. 6, 435–446, 2005.

[59] Wang, F., D. Banerjee, Y. Liu, X. Chen, and X. Liu, "Upconversion nanoparticles in biological labeling, imaging, and therapy," *Analyst*, Vol. 135, No. 8, 1839–1854, 2010.

[60] Lakowicz, J. R., C. D. Geddes, I. Gryczynski, J. Malicka, Z. Gryczynski, K. Aslan, J. Lukomska, E. Matveeva, J. Zhang, R. Badugu, and J. Huang, "Advances in surface-enhanced fluorescence," *Journal of Fluorescence*, Vol. 14, 425–441, 2004.

[61] Sultangaziyev, A. and R. Bukasov, "Applications of surface-enhanced fluorescence (SEF) spectroscopy in bio-detection and biosensing," *Sensing and Bio-Sensing Research*, Vol. 30, 100382, 2020.

[62] Jeong, Y., Y.-M. Kook, K. Lee, and W.-G. Koh, "Metal enhanced fluorescence (MEF) for biosensors: General approaches and a review of recent developments," *Biosensors and Bioelectronics*, Vol. 111, 102–116, 2018.

[63] Beliaev, L. Y., O. Takayama, P. N. Melentiev, and A. V. Lavrinenko, "Photoluminescence control by hyperbolic metamaterials and metasurfaces: A review," *Opto-Electronic Advances*, Vol. 4, No. 8, 210031, 2021.

[64] Aslan, K., I. Gryczynski, J. Malicka, E. Matveeva, J. R. Lakowicz, and C. D. Geddes, "Metal-enhanced fluorescence: An emerging tool in biotechnology," *Current Opinion in Biotechnology*, Vol. 16, No. 1, 55–62, 2005.

[65] Shkondin, E., T. Repän, M. E. A. Panah, A. V. Lavrinenko, and O. Takayama, "High aspect ratio plasmonic nanotrench structures with large active surface area for label-free mid-infrared molecular absorption sensing," *ACS Applied Nano Materials*, Vol. 1, No. 3, 1212–1218, 2018.

[66] Sun, T., S. Kan, G. Marriott, and C. Chang-Hasnain, "High-contrast grating resonators for label-free detection of disease biomarkers," *Scientific Reports*, Vol. 6, No. 1, 27482, 2016.

[67] Miles, A. J. and B. A. Wallace, "Circular dichroism spectroscopy of membrane proteins," *Chemical Society Reviews*, Vol. 45, No. 18, 4859–4872, 2016.

[68] McMeekin, T. L., M. L. Groves, and N. J. Hipp, "Refractive indices of amino acids, proteins, and related substances," in *Amino Acids and Serum Proteins*, Vol. 25, 54–66, ACS Publications, 1964.

[69] Pawley, J. B., *Handbook of Biological Confocal Microscopy*, 3rd ed., 368–380, Springer Science + Business Media, LLC, New York, 2006.

[70] Berke, I. M., J. P. Miola, M. A. David, M. K. Smith, and C. Price, "Seeing through musculoskeletal tissues: Improving in situ imaging of bone and the lacunar canalicular system through optical clearing," *PLoS One*, Vol. 11, No. 3, e0150268, 2016.

[71] Khan, R., B. Gul, S. Khan, H. Nisar, and I. Ahmad, "Refractive index of biological tissues: Review, measurement techniques, and applications," *Photodiagnosis and Photodynamic Therapy*, Vol. 33, 102192, 2021.

[72] Zhou, Y., M. Luo, X. Zhao, Y. Li, Q. Wang, Z. Liu, J. Guo, Z. Guo, J. Liu, and X. Wu, "Asymmetric tetramer metasurface sensor governed by quasi-bound states in the continuum," *Nanophotonics*, Vol. 12, No. 7, 1295–1307, 2023.

[73] Taleuzzaman, M., "Limit of blank (LOB), limit of detection (LOD), and limit of quantification (LOQ)," *Organic & Medicinal Chemistry*, Vol. 7, 1–5, 2018.

[74] Shrivastava, A. and V. Gupta, "Methods for the determination of limit of detection and limit of quantitation of the analytical methods," *Chronicles of Young Scientists*, Vol. 2, No. 1, 21–25, 2011.

[75] Baffou, G. and R. Quidant, "Thermo-plasmonics: Using metallic nanostructures as nano-sources of heat," *Laser & Photonics Reviews*, Vol. 7, No. 2, 171–187, 2013.

[76] Lalisse, A., G. Tessier, J. Plain, and G. Baffou, "Quantifying the efficiency of plasmonic materials for near-field enhancement and photothermal conversion," *The Journal of Physical Chemistry C*, Vol. 119, No. 45, 25 518–25 528, 2015.

[77] Takayama, O., "High aspect ratio nanostructures for photothermal applications," in *Thermal Plasmonics and Metamaterials for a Low-Carbon Society*, K. Kajikawa and J. Takahara, eds., 1st Edition, Chapter 3, 39-58, CRC Press, Boca Raton, 2024.

[78] Guler, U., J. C. Ndukaife, G. V. Naik, A. G. A. Nnanna, A. V. Kildishev, V. M. Shalaev, and A. Boltasseva, "Local heating with titanium nitride nanoparticles," in *Nano Letters*, Vol. 13, 6078–6083, 2013.

[79] Ishii, S., M. Higashino, S. Goya, E. Shkondin, K. Tanaka, T. Nagao, O. Takayama, and S. Murai, "Extreme thermal anisotropy in high-aspect-ratio titanium nitride nanostructures for efficient photothermal heating," *Nanophotonics*, Vol. 10, No. 5, 1487–1494, 2021.

[80] Daimon, M. and A. Masumura, "Measurement of the refractive index of distilled water from the near-infrared region to the ultraviolet region," *Applied Optics*, Vol. 46, No. 18, 3811–3820, 2007.

[81] Langer, J., D. J. de Aberasturi, J. Aizpurua, R. A. Alvarez-Puebla, B. Auguié, J. J. Baumberg, G. C. Bazan, S. E. J. Bell, A. Boisen, A. G. Brolo, *et al.*, "Present and future of surface-enhanced Raman scattering," *ACS Nano*, Vol. 14, No. 1, 28–117, 2020.

[82] Mitra, S. and M. Basak, "Diverse bio-sensing and therapeutic applications of plasmon enhanced nanostructures," *Materials Today*, Vol. 57, 225–261, 2022.

[83] Takayama, O., "Mid-infrared nanophotonics for biochemical sensing," *Romanian Report in Physics*, Vol. 72, 408, 2020.

[84] Wang, J., Z. Xie, Y. Zhu, P. Zeng, S. He, J. Wang, H. Wei, and C. Yu, "Surface-enhanced infrared absorption spectroscopy (SEIRAS) for biochemical analysis: Progress and perspective," *Trends in Environmental Analytical Chemistry*, Vol. 41, e00226, 2024.

[85] Li, P., G. Kang, X. Meng, and X. Tan, "Iridium nanopillars with multilayered, uniformly distributed hot spots for highly reproducible surface-enhanced Raman scattering," in *2015 IEEE 15th International Conference on Nanotechnology (IEEE-NANO)*, 649–653, Rome, Italy, 2015.

[86] Pyrak, E., A. Szaniawska, and A. Kudelski, "Applications of sers in biochemical and medical analysis," in *Molecular and Laser Spectroscopy: Advances and Applications*, Vol. 3, 375–408, Elsevier, 2022.

[87] Issatayeva, A., E. Farnesi, D. Cialla-May, M. Schmitt, F. M. A. Rizzi, D. Milanese, S. Selleri, and A. Cucinotta, "SERS-based methods for the detection of genomic biomarkers of cancer," *Talanta*, Vol. 267, 125198, 2024.

[88] Taguchi, A., "Plasmonic tip for nano Raman microcopy: Structures, materials, and enhancement," *Optical Review*, Vol. 24, No. 3, 462–469, 2017.

[89] Naik, G. V., J. Kim, and A. Boltasseva, "Oxides and nitrides as alternative plasmonic materials in the optical range," *Optical Materials Express*, Vol. 1, No. 6, 1090–1099, 2011.

[90] Dasog, M., "Transition metal nitrides are heating up the field of plasmonics," *Chemistry of Materials*, Vol. 34, No. 10, 4249–4258, 2022.

[91] Kumar, M., N. Umezawa, S. Ishii, and T. Nagao, "Examining the performance of refractory conductive ceramics as plasmonic materials: A theoretical approach," *ACS Photonics*, Vol. 3, No. 1, 43–50, 2016.

[92] Sugavaneshwar, R. P., S. Ishii, T. D. Dao, A. Ohi, T. Nabatame, and T. Nagao, "Fabrication of highly metallic TiN films by pulsed laser deposition method for plasmonic applications," *ACS Photonics*, Vol. 5, No. 3, 814–819, 2018.

[93] Judek, J., P. Wróbel, P. P. Michałowski, M. Ożga, B. Witkowski, A. Seweryn, M. Struzik, C. Jastrzębski, and K. Zberecki, "Titanium nitride as a plasmonic material from near-ultraviolet to very-long-wavelength infrared range," *Materials*, Vol. 14, No. 22, 7095, 2021.

[94] Beliaev, L. Y., E. Shkondin, A. V. Lavrinenko, and O. Takayama, "Optical properties of plasmonic titanium ni-

tride thin films from ultraviolet to mid-infrared wavelengths deposited by pulsed-DC sputtering, thermal and plasma-enhanced atomic layer deposition," *Optical Materials*, Vol. 143, 114237, 2023.

[95] Patsalas, P., "Zirconium nitride: A viable candidate for photonics and plasmonics?" *Thin Solid Films*, Vol. 688, 137438, 2019.

[96] El-Saeed, A. H. and N. K. Allam, "Refractory plasmonics: Orientation-dependent plasmonic coupling in TiN and ZrN nanocubes," *Physical Chemistry Chemical Physics*, Vol. 20, No. 3, 1881–1888, 2018.

[97] Gueddaoui, H., S. Maabed, G. Schmerber, M. Guemmaz, and J. C. Parlebas, "Structural and optical properties of vanadium and hafnium nitride nanoscale films: Effect of stoichiometry," *The European Physical Journal B*, Vol. 60, 305–312, 2007.

[98] Lan, L., H. Yao, G. Li, X. Fan, M. Li, and T. Qiu, "Structural engineering of transition-metal nitrides for surface-enhanced Raman scattering chips," *Nano Research*, Vol. 15, 3794–3803, 2022.

[99] Sheta, E. M. and P. K. Choudhury, "Vanadium nitride-based ultra-wideband nearly perfect metamaterial absorber," *Journal of Nanophotonics*, Vol. 15, No. 3, 036007, 2021.

[100] Karl, P., M. Ubl, M. Hentschel, P. Flad, Z.-Y. Chiao, J.-W. Yang, Y.-J. Lu, and H. Giessen, "Optical properties of niobium nitride plasmonic nanoantennas for the near-and mid-infrared spectral range," *Optical Materials Express*, Vol. 10, No. 10, 2597–2606, 2020.

[101] Huang, W., Y. Gao, J. Wang, P. Ding, M. Yan, F. Wu, J. Liu, D. Liu, C. Guo, B. Yang, and W. Cao, "Plasmonic enhanced reactive oxygen species activation on low-work-function tungsten nitride for direct near-infrared driven photocatalysis," *Small*, Vol. 16, No. 45, 2004557, 2020.

[102] Zhong, Y., X. Xia, F. Shi, J. Zhan, J. Tu, and H. J. Fan, "Transition metal carbides and nitrides in energy storage and conversion," *Advanced Science*, Vol. 3, No. 5, 1500286, 2016.

[103] Chiao, Z.-Y., Y.-C. Chen, J.-W. Chen, Y.-C. Chu, J.-W. Yang, T.-Y. Peng, W.-R. Syong, H. W. H. Lee, S.-W. Chu, and Y.-J. Lu, "Full-color generation enabled by refractory plasmonic crystals," *Nanophotonics*, Vol. 11, No. 12, 2891–2899, 2022.

[104] Das, P., B. Biswas, K. C. Maurya, M. Garbrecht, and B. Saha, "Refractory plasmonic hafnium nitride and zirconium nitride thin films as alternatives to silver for solar mirror applications," *ACS Applied Materials & Interfaces*, Vol. 14, No. 41, 46 708–46 715, 2022.

[105] Silveirinha, M. and N. Engheta, "Tunneling of electromagnetic energy through subwavelength channels and bends using ε-near-zero materials," *Physical Review Letters*, Vol. 97, No. 15, 157403, 2006.

[106] Engheta, N., "Pursuing near-zero response," *Science*, Vol. 340, No. 6130, 286–287, 2013.

[107] Braic, L., N. Vasilantonakis, A. Mihai, I. J. V. Garcia, S. Fearn, B. Zou, N. M. Alford, B. Doiron, R. F. Oulton, S. A. Maier, *et al.*, "Titanium oxynitride thin films with tunable double epsilon-near-zero behavior for nanophotonic applications," *ACS Applied Materials & Interfaces*, Vol. 9, No. 35, 29 857–29 862, 2017.

[108] Shabani, A., M. T. Korsa, S. Petersen, M. K. Nezhad, Y. K. Mishra, and J. Adam, "Zirconium nitride: Optical properties of an emerging intermetallic for plasmonic applications," *Advanced Photonics Research*, Vol. 2, No. 11, 2100178, 2021.

[109] Shkondin, E., T. Repän, O. Takayama, and A. V. Lavrinenko, "High aspect ratio titanium nitride trench structures as plasmonic biosensor," *Optical Materials Express*, Vol. 7, No. 11, 4171–4182, 2017.

[110] Beliaev, L. Y., E. Shkondin, A. V. Lavrinenko, and O. Takayama, "Titanium nitride nanotrench metasurfaces for mid-infrared chemical sensing," *ACS Applied Optical Materials*, Vol. 2, No. 1, 88–96, 2024.

[111] Surre, F., O. D. Bernal, H.-C. Seat, and J. H. Sharp, "Estimation of transition metal nitride surface plasmon refractometer sensitivity," in *2019 IEEE Sensors*, 1–4, Montreal, QC, Canada, 2019.

[112] Shishodia, M. S. and P. Pathania, "Estimation of sensing characteristics for refractory nitrides based gain assisted core-shell plasmonic nanoparticles," *Physics of Plasmas*, Vol. 25, No. 4, 042101, 2018.

[113] Elsayed, A. M., A. M. Ahmed, and A. H. Aly, "Glucose sensor modeling based on fano resonance excitation in titania nanotube photonic crystal coated by titanium nitride as a plasmonic material," *Applied Optics*, Vol. 61, No. 7, 1668–1674, 2022.

[114] Tathfif, I., K. S. Rashid, A. A. Yaseer, and R. H. Sagor, "Alternative material titanium nitride based refractive index sensor embedded with defects: An emerging solution in sensing arena," *Results in Physics*, Vol. 29, 104795, 2021.

[115] Khalil, A. E., A. H. El-Saeed, M. A. Ibrahim, M. E. Hashish, M. R. Abdelmonem, M. F. O. Hameed, M. Y. Azab, and S. S. A. Obayya, "Highly sensitive photonic crystal fiber biosensor based on titanium nitride," *Optical and Quantum Electronics*, Vol. 50, 158, 2018.

[116] Kaur, V. and S. Singh, "Design of titanium nitride coated PCF-SPR sensor for liquid sensing applications," *Optical Fiber Technology*, Vol. 48, 159–164, 2019.

[117] Monfared, Y. E., "Refractive index sensor based on surface plasmon resonance excitation in a D-shaped photonic crystal fiber coated by titanium nitride," *Plasmonics*, Vol. 15, 535–542, 2020.

[118] Monfared, Y. E., B. L. Kurylyk, and M. Dasog, "Highly sensitive plasmonic fiber-optic sensors using group IV transition metal nitrides: A numerical investigation," *Plasmonics*, Vol. 17, 931–940, 2022.

[119] Monfared, Y. E. and M. Dasog, "Computational investigation of the plasmonic properties of TiN, ZrN, and HfN nanoparticles: The role of particle size, medium, and surface oxidation," *Canadian Journal of Chemistry*, Vol. 99, No. 7, 576–584, 2021.

[120] Rakić, A. D., A. B. Djurišić, J. M. Elazar, and M. L. Majewski, "Optical properties of metallic films for vertical-cavity optoelectronic devices," *Applied Optics*, Vol. 37, No. 22, 5271–5283, 1998.

[121] Qiu, G., S. P. Ng, and C.-M. L. Wu, "Label-free surface plasmon resonance biosensing with titanium nitride thin film," *Biosensors and Bioelectronics*, Vol. 106, 129–135, 2018.

[122] Soler, M. and L. M. Lechuga, "Biochemistry strategies for label-free optical sensor biofunctionalization: Advances towards real applicability," *Analytical and Bioanalytical Chemistry*, Vol. 414, No. 18, 5071–5085, 2022.

[123] Qiu, G., A. Thakur, C. Xu, S.-P. Ng, Y. Lee, and C.-M. L. Wu, "Detection of glioma-derived exosomes with the biotinylated antibody-functionalized titanium nitride plasmonic biosensor," *Advanced Functional Materials*, Vol. 29, No. 9, 1806761, 2019.

[124] Wang, X., X. Ma, E. Shi, P. Lu, L. Dou, X. Zhang, and H. Wang, "Large-scale plasmonic hybrid framework with built-in nanohole array as multifunctional optical sensing platforms," *Small*, Vol. 16, No. 11, 1906459, 2020.

[125] Xu, C., G. Qiu, S. P. Ng, and C.-M. L. Wu, "Nanostructured titanium nitride for highly sensitive localized surface plasmon resonance biosensing," *Ceramics International*, Vol. 46,

No. 13, 20 993–20 999, 2020.

[126] Reiter, S., W. Han, C. Mai, D. Spirito, J. Jose, M. Zöllner, O. Fursenko, M. A. Schubert, I. Stemmler, C. Wenger, and I. A. Fischer, "Titanium nitride plasmonic nanohole arrays for cmos-compatible integrated refractive index sensing: influence of layer thickness on optical properties," *Plasmonics*, Vol. 18, 831–843, 2023.

[127] Han, W., S. Reiter, J. Schlipf, C. Mai, D. Spirito, J. Jose, C. Wenger, and I. A. Fischer, "Strongly enhanced sensitivities of CMOS compatible plasmonic titanium nitride nanohole arrays for refractive index sensing under oblique incidence," *Optics Express*, Vol. 31, No. 11, 17 389–17 407, 2023.

[128] Günaydın, B. N., M. Gülmez, M. Torabfam, Z. S. Pehlivan, A. Tütüncüoğlu, C. I. Kayalan, E. Saatçioğlu, M. K. Bayazıt, M. Yüce, and H. Kurt, "Plasmonic titanium nitride nanohole arrays for refractometric sensing," *ACS Applied Nano Materials*, Vol. 6, No. 22, 20 612–20 622, 2023.

[129] Asencios, J., R. Moro, C. Luyo, and A. Talledo, "High sensitive biosensors based on the coupling between surface plasmon polaritons on titanium nitride and a planar waveguide mode," *Sensors*, Vol. 20, No. 6, 1784, 2020.

[130] Juneja, S. and M. S. Shishodia, "Surface plasmon amplification in refractory transition metal nitrides based nanoparticle dimers," *Optics Communications*, Vol. 433, 89–96, 2019.

[131] Fu, T., Y. Chen, C. Du, W. Yang, R. Zhang, L. Sun, and D. Shi, "Numerical investigation of plasmon sensitivity and surface-enhanced Raman scattering enhancement of individual TiN nanosphere multimers," *Nanotechnology*, Vol. 31, No. 13, 135210, 2020.

[132] Rong, W., C. Du, M. Lei, X. Zhang, Y. Ding, X. Li, and D. Shi, "Adjustment of eccentricity and split angle for improved SERS and refractive index sensing of TiN nanodonuts," *Physica Scripta*, Vol. 98, No. 4, 045019, 2023.

[133] Sucheewa, N., W. Wongwiriyapan, A. Klamchuen, M. Obata, M. Fujishige, K. Takeuchi, T. Lertvanithphol, T. Wutikhun, S. Kullyakool, W. Auttasiri, *et al.*, "Tailoring properties of hafnium nitride thin film via reactive gas-timing RF magnetron sputtering for surface enhanced-Raman scattering substrates," *Crystals*, Vol. 12, No. 1, 78, 2022.

[134] Kaisar, N., Y.-T. Huang, S. Jou, H.-F. Kuo, B.-R. Huang, C.-C. Chen, Y.-F. Hsieh, and Y.-C. Chung, "Surface-enhanced Raman scattering substrates of flat and wrinkly titanium nitride thin films by sputter deposition," *Surface and Coatings Technology*, Vol. 337, 434–438, 2018.

[135] Wei, H., M. Wu, Z. Dong, Y. Chen, J. Bu, J. Lin, Y. Yu, Y. Wei, Y. Cui, and R. Wang, "Composition, microstructure and SERS properties of titanium nitride thin film prepared via nitridation of sol-gel derived titania thin films," *Journal of Raman Spectroscopy*, Vol. 48, No. 4, 578–585, 2017.

[136] Rajesh, Y., M. S. S. Bharati, S. V. Rao, and M. G. Krishna, "ZnO nanowire arrays decorated with titanium nitride nanoparticles as surface-enhanced Raman scattering substrates," *Applied Physics A*, Vol. 127, No. 4, 270, 2021.

[137] Jen, Y.-J., M.-J. Lin, H.-L. Cheang, and T.-L. Chan, "Obliquely deposited titanium nitride nanorod arrays as surface-enhanced Raman scattering substrates," *Sensors*, Vol. 19, No. 21, 4765, 2019.

[138] Zhao, J., J. Lin, H. Wei, X. Li, W. Zhang, G. Zhao, J. Bu, and Y. Chen, "Surface enhanced Raman scattering substrates based on titanium nitride nanorods," *Optical Materials*, Vol. 47, 219–224, 2015.

[139] Esmaeilzadeh, M., H. Dizajghorbani-Aghdam, and R. Malekfar, "Surface-enhanced Raman scattering of methylene blue on titanium nitride nanoparticles synthesized by laser ablation in organic solvents," *Spectrochimica Acta, Part A: Molecular and Biomolecular Spectroscopy*, Vol. 257, 119721, 2021.

[140] Mishra, P., A. K. Debnath, and S. D. Choudhury, "Titanium nitride as an alternative and reusable plasmonic substrate for fluorescence coupling," *Physical Chemistry Chemical Physics*, Vol. 24, No. 10, 6256–6265, 2022.

[141] Kamakura, R., S. Murai, K. Fujita, and K. Tanaka, "Enhanced photoluminescence from organic dyes coupled to periodic array of zirconium nitride nanoparticles," *ACS Photonics*, Vol. 5, No. 8, 3057–3063, 2018.

[142] Kamakura, R., S. Murai, S. Ishii, T. Nagao, K. Fujita, and K. Tanaka, "Plasmonic-photonic hybrid modes excited on a titanium nitride nanoparticle array in the visible region," *ACS Photonics*, Vol. 4, No. 4, 815–822, 2017.

[143] Noginov, M. A., L. Gu, J. Livenere, G. Zhu, A. K. Pradhan, R. Mundle, M. Bahoura, Y. A. Barnakov, and V. A. Podolskiy, "Transparent conductive oxides: Plasmonic materials for telecom wavelengths," *Applied Physics Letters*, Vol. 99, No. 2, 021101, 2011.

[144] Kim, D.-H., M.-R. Park, H.-J. Lee, and G.-H. Lee, "Thickness dependence of electrical properties of ITO film deposited on a plastic substrate by RF magnetron sputtering," *Applied Surface Science*, Vol. 253, No. 2, 409–411, 2006.

[145] Lee, M.-J., J. Lim, J. Bang, W. Lee, and J.-M. Myoung, "Effect of the thickness and hydrogen treatment on the properties of Ga-doped ZnO transparent conductive films," *Applied Surface Science*, Vol. 255, No. 5, 3195–3200, 2008.

[146] Minami, T., T. Miyata, Y. Ohtani, and T. Kuboi, "Effect of thickness on the stability of transparent conducting impurity-doped ZnO thin films in a high humidity environment," *Physica Status Solidi — Rapid Research Letters*, Vol. 1, No. 1, R31–R33, 2007.

[147] Cao, B.-W., C. Li, W.-J. Shi, C.-Q. Han, Y. Wu, and C.-C. Yan, "Large-area mid-infrared broadband absorbers based on spiral ITO resulting from the combination of two different broadening absorption methods," *Optics Express*, Vol. 29, No. 21, 34 427–34 440, 2021.

[148] Wang, C.-N., Y.-L. Li, F.-L. Gong, Y.-H. Zhang, S.-M. Fang, and H.-L. Zhang, "Advances in doped ZnO nanostructures for gas sensor," *The Chemical Record*, Vol. 20, No. 12, 1553–1567, 2020.

[149] Pineda-Reyes, A. M., M. R. Herrera-Rivera, H. Rojas-Chávez, H. Cruz-Martínez, and D. I. Medina, "Recent advances in ZnO-based carbon monoxide sensors: Role of doping," *Sensors*, Vol. 21, No. 13, 4425, 2021.

[150] Chu, S., Y. Liang, M. Lu, H. Yuan, Y. Han, J.-F. Masson, and W. Peng, "Mode-coupling generation using ITO nanodisk arrays with Au substrate enabling narrow-band biosensing," *Biosensors*, Vol. 13, No. 6, 649, 2023.

[151] Mishra, S. K. and B. D. Gupta, "Surface plasmon resonance based fiber optic pH sensor utilizing Ag/ITO/Al/hydrogel layers," *Analyst*, Vol. 138, No. 9, 2640–2646, 2013.

[152] Wang, Q., B. Sun, E. Hu, and W. Wei, "Cu/ITO-coated uncladded fiber-optic biosensor based on surface plasmon resonance," *IEEE Photonics Technology Letters*, Vol. 31, No. 14, 1159–1162, 2019.

[153] Prieto-Cortés, P., R. I. Álvarez Tamayo, M. García-Méndez, and M. Durán-Sánchez, "Lossy mode resonance generation on sputtered aluminum-doped zinc oxide thin films deposited on multimode optical fiber structures for sensing applications in the 1.55 µm wavelength range," *Sensors*, Vol. 19, No. 19, 4189, 2019.

[154] Ozcariz, A., D. A. Piña-Azamar, C. R. Zamarreño, R. Dominguez, and F. J. Arregui, "Aluminum doped zinc oxide (AZO) coated optical fiber LMR refractometers — An experimental demonstration," *Sensors and Actuators B: Chemical*, Vol. 281, 698–704, 2019.

[155] Tien, C.-L., T.-C. Mao, and C.-Y. Li, "Lossy mode resonance sensors fabricated by RF magnetron sputtering GZO thin film and D-shaped fibers," *Coatings*, Vol. 10, No. 1, 29, 2020.

[156] Joseph, S., S. Sarkar, and J. Joseph, "High-sensitivity resonant cavity modes excited in a low contrast grating layer with large aspect-ratio," *IEEE Sensors Journal*, Vol. 22, No. 17, 16 856–16 861, 2022.

[157] Chatterjee, S., E. Shkondin, O. Takayama, A. Fisher, A. Fraiwan, U. A. Gurkan, A. V. Lavrinenko, and G. Strangi, "Hydrogen gas sensing using aluminum doped ZnO metasurfaces," *Nanoscale Advances*, Vol. 2, No. 8, 3452–3459, 2020.

[158] Kumar, R., A. Umar, D. S. Rana, P. Sharma, M. S. Chauhan, and S. Chauhan, "Fe-doped ZnO nanoellipsoids for enhanced photocatalytic and highly sensitive and selective picric acid sensor," *Materials Research Bulletin*, Vol. 102, 282–288, 2018.

[159] Ghosh, J., R. Ghosh, and P. K. Giri, "Tuning the visible photoluminescence in Al doped ZnO thin film and its application in label-free glucose detection," *Sensors and Actuators B: Chemical*, Vol. 254, 681–689, 2018.

[160] Mishra, S. K., D. Kumari, and B. D. Gupta, "Surface plasmon resonance based fiber optic ammonia gas sensor using ITO and polyaniline," *Sensors and Actuators B: Chemical*, Vol. 171-172, 976–983, 2012.

[161] Mishra, S. K. and B. D. Gupta, "Surface plasmon resonance-based fiber-optic hydrogen gas sensor utilizing indium-tin oxide (ITO) thin films," *Plasmonics*, Vol. 7, 627–632, 2012.

[162] Mishra, S. K., S. Bhardwaj, and B. D. Gupta, "Surface plasmon resonance-based fiber optic sensor for the detection of low concentrations of ammonia gas," *IEEE Sensors Journal*, Vol. 15, No. 2, 1235–1239, 2015.

[163] Ohodnicki, P. R., C. Wang, and M. Andio, "Plasmonic transparent conducting metal oxide nanoparticles and nanoparticle films for optical sensing applications," *Thin Solid Films*, Vol. 539, 327–336, 2013.

[164] Sturaro, M., E. D. Gaspera, C. Cantalini, M. Guglielmi, and A. Martucci, "Near infrared plasmonic gas sensing with doped metal oxide nanocrystals," in *Proceedings of Eurosensors 2017*, Vol. 1, No. 4, 319, Paris, France, 2017.

[165] Alsaif, M. M. Y. A., M. R. Field, T. Daeneke, A. F. Chrimes, W. Zhang, B. J. Carey, K. J. Berean, S. Walia, J. V. Embden, B. Zhang, *et al.*, "Exfoliation solvent dependent plasmon resonances in two-dimensional sub-stoichiometric molybdenum oxide nanoflakes," *ACS Applied Materials & Interfaces*, Vol. 8, No. 5, 3482–3493, 2016.

[166] Liu, W., Q. Xu, W. Cui, C. Zhu, and Y. Qi, "CO2-assisted fabrication of two-dimensional amorphous molybdenum oxide nanosheets for enhanced plasmon resonances," *Angewandte Chemie International Edition*, Vol. 56, No. 6, 1600–1604, 2017.

[167] Zhang, N. M. Y., K. Li, T. Zhang, P. Shum, Z. Wang, Z. Wang, N. Zhang, J. Zhang, T. Wu, and L. Wei, "Electron-rich two-dimensional molybdenum trioxides for highly integrated plasmonic biosensing," *ACS Photonics*, Vol. 5, No. 2, 347–352, 2018.

[168] Zhang, B. Y., A. Zavabeti, A. F. Chrimes, F. Haque, L. A. O'Dell, H. Khan, N. Syed, R. Datta, Y. Wang, A. S. R. Chesman, *et al.*, "Degenerately hydrogen doped molybdenum oxide nanodisks for ultrasensitive plasmonic biosensing," *Advanced Functional Materials*, Vol. 28, No. 11, 1706006, 2018.

[169] Ren, G., B. Y. Zhang, Q. Yao, A. Zavabeti, C. S. Huertas, R. Brkljača, M. W. Khan, H. Nili, R. S. Datta, H. Khan, *et al.*, "An ultrasensitive silicon photonic ion sensor enabled by 2D plasmonic molybdenum oxide," *Small*, Vol. 15, No. 9, 1805251, 2019.

[170] Chen, K., P. Guo, T. D. Dao, S.-Q. Li, S. Ishii, T. Nagao, and R. P. H. Chang, "Protein-functionalized indium-tin oxide nanoantenna arrays for selective infrared biosensing," *Advanced Optical Materials*, Vol. 5, No. 17, 1700091, 2017.

[171] Li, S. Q., P. Guo, L. Zhang, W. Zhou, T. W. Odom, T. Seideman, J. B. Ketterson, and R. P. H. Chang, "Infrared plasmonics with indium-tin-oxide nanorod arrays," *ACS Nano*, Vol. 5, No. 11, 9161–9170, 2011.

[172] Shkondin, E., O. Takayama, M. E. A. Panah, P. Liu, P. V. Larsen, M. D. Mar, F. Jensen, and A. V. Lavrinenko, "Large-scale high aspect ratio Al-doped ZnO nanopillars arrays as anisotropic metamaterials," *Optical Materials Express*, Vol. 7, No. 5, 1606–1627, 2017.

[173] Takayama, O., E. Shkondin, A. Bodganov, M. E. A. Panah, K. Golenitskii, P. Dmitriev, T. Repän, R. Malureanu, P. Belov, F. Jensen, and A. V. Lavrinenko, "Midinfrared surface waves on a high aspect ratio nanotrench platform," *ACS Photonics*, Vol. 4, No. 11, 2899–2907, 2017.

[174] Takayama, O., P. Dmitriev, E. Shkondin, O. Yermakov, M. Panah, K. Golenitskii, F. Jensen, A. Bogdanov, and A. Lavrinenko, "Experimental observation of Dyakonov plasmons in the mid-infrared," *Semiconductors*, Vol. 52, 442–446, 2018.

[175] Wang, Y., M. Zhang, H. Ma, H. Su, A. Li, W. Ruan, and B. Zhao, "Surface plasmon resonance from gallium-doped zinc oxide nanoparticles and their electromagnetic enhancement contribution to surface-enhanced Raman scattering," *ACS Applied Materials & Interfaces*, Vol. 13, No. 29, 35 038–35 045, 2021.

[176] Tian, J., C. Xu, S. Cui, L. Ma, and Y. Fu, "A photonic crystal fiber-based biosensor with quasi-D-shaped layout and ITO-graphene combination," *Plasmonics*, Vol. 16, 1451–1460, 2021.

[177] Liu, C., J. Wang, F. Wang, W. Su, L. Yang, J. Lv, G. Fu, X. Li, Q. Liu, T. Sun, and P. K. Chu, "Surface plasmon resonance (SPR) infrared sensor based on D-shape photonic crystal fibers with ITO coatings," *Optics Communications*, Vol. 464, 125496, 2020.

[178] Islam, M. R., A. N. M. Iftekher, F. Noor, M. R. H. Khan, M. T. Reza, and M. M. Nishat, "AZO-coated plasmonic PCF nanosensor for blood constituent detection in near-infrared and visible spectrum," *Applied Physics A: Materials Science and Processing*, Vol. 128, No. 1, 86, 2022.

[179] Yang, W., J. Yu, X. Xi, Y. Sun, Y. Shen, W. Yue, C. Zhang, and S. Jiang, "Preparation of graphene/ITO nanorod metamaterial/U-bent-annealing fiber sensor and DNA biomolecule detection," *Nanomaterials*, Vol. 9, No. 8, 1154, 2019.

[180] Hu, Y., B. Y. Zhang, F. Haque, G. Ren, and J. Z. Ou, "Plasmonic metal oxides and their biological applications," *Materials Horizons*, Vol. 9, 2288–2324, 2022.

[181] Patil, M. K., S. H. Gaikwad, and S. P. Mukherjee, "Phase- and morphology-controlled synthesis of tunable plasmonic MoO3-x nanomaterials for ultrasensitive surface-enhanced Raman spectroscopy detection," *The Journal of Physical Chemistry C*, Vol. 124, No. 38, 21 082–21 093, 2020.

[182] Paliwal, A., A. Sharma, M. Tomar, and V. Gupta, "Optical properties of WO3 thin films using surface plasmon reso-

nance technique," *Journal of Applied Physics*, Vol. 115, No. 4, 043104, 2014.

[183] Gordon, T. R., M. Cargnello, T. Paik, F. Mangolini, R. T. Weber, P. Fornasiero, and C. B. Murray, "Nonaqueous synthesis of TiO2 nanocrystals using TiF4 to engineer morphology, oxygen vacancy concentration, and photocatalytic activity," *Journal of the American Chemical Society*, Vol. 134, No. 15, 6751–6761, 2012.

[184] Gu, C., D. Li, S. Zeng, T. Jiang, X. Shen, and H. Zhang, "Synthesis and defect engineering of molybdenum oxides and their SERS applications," *Nanoscale*, Vol. 13, No. 11, 5620–5651, 2021.

[185] Du, X., D. Liu, K. An, S. Jiang, Z. Wei, S. Wang, W. F. Ip, and H. Pan, "Advances in oxide semiconductors for surface enhanced Raman scattering," *Applied Materials Today*, Vol. 29, 101563, 2022.

[186] Song, X., M. Yin, J. Li, Y. Li, H. Yang, Q. Kong, H. Bai, G. Xi, and L. Mao, "Moving MoO2/C nanospheres with the functions of enrichment and sensing for online-high-throughput SERS detection," *Analytical Chemistry*, Vol. 94, No. 19, 7029–7034, 2022.

[187] Wang, J., Y. Yang, H. Li, J. Gao, P. He, L. Bian, F. Dong, and Y. He, "Stable and tunable plasmon resonance of molybdenum oxide nanosheets from the ultraviolet to the near-infrared region for ultrasensitive surface-enhanced Raman analysis," *Chemical Science*, Vol. 10, No. 25, 6330–6335, 2019.

[188] Li, P., L. Zhu, C. Ma, L. Zhang, L. Guo, Y. Liu, H. Ma, and B. Zhao, "Plasmonic molybdenum tungsten oxide hybrid with surface-enhanced Raman scattering comparable to that of noble metals," *ACS Applied Materials & Interfaces*, Vol. 12, No. 16, 19 153–19 160, 2020.

[189] Liu, W., H. Bai, X. Li, W. Li, J. Zhai, J. Li, and G. Xi, "Improved surface-enhanced Raman spectroscopy sensitivity on metallic tungsten oxide by the synergistic effect of surface plasmon resonance coupling and charge transfer," *The Journal of Physical Chemistry Letters*, Vol. 9, No. 14, 4096–4100, 2018.

[190] Zhang, L., G. Wei, J. Li, M. Yin, and G. Xi, "Plasmonic molybdenum dioxide ultrathin nanowire bundles for highly sensitive, stable, and reproducible surface-enhanced Raman spectroscopy," *The Journal of Physical Chemistry C*, Vol. 127, No. 13, 6439–6445, 2023.

[191] Zhang, Q., X. Li, W. Yi, W. Li, H. Bai, J. Liu, and G. Xi, "Plasmonic MoO2 nanospheres as a highly sensitive and stable non-noble metal substrate for multicomponent surface-enhanced Raman analysis," *Analytical Chemistry*, Vol. 89, No. 21, 11 765–11 771, 2017.

[192] Zhou, X., X. Zhao, F. Xie, Z. Jin, X. Song, W. Xie, X. Wang, and Z. Tang, "Plasmonic hybrid Mo/MoO2 nanospheres as surface-enhanced Raman scattering substrates for molecular detection," *ACS Applied Nano Materials*, Vol. 3, No. 6, 5656–5664, 2020.

[193] Zheng, Z., N. Xu, S. L. Oscurato, M. Tamagnone, F. Sun, Y. Jiang, Y. Ke, J. Chen, W. Huang, W. L. Wilson, *et al.*, "A mid-infrared biaxial hyperbolic van der Waals crystal," *Science Advances*, Vol. 5, No. 5, eaav8690, 2019.

[194] Kumamoto, Y., A. Taguchi, and S. Kawata, "Deep-ultraviolet biomolecular imaging and analysis," *Advanced Optical Materials*, Vol. 7, No. 5, 1801099, 2019.

[195] Barulin, A., J.-B. Claude, S. Patra, N. Bonod, and J. Wenger, "Deep ultraviolet plasmonic enhancement of single protein autofluorescence in zero-mode waveguides," *Nano Letters*, Vol. 19, No. 10, 7434–7442, 2019.

[196] Maidecchi, G., G. Gonella, R. P. Zaccaria, R. Moroni, L. Anghinolfi, A. Giglia, S. Nannarone, L. Mattera, H.-L. Dai, M. Canepa, and F. Bisio, "Deep ultraviolet plasmon resonance in aluminum nanoparticle arrays," *ACS Nano*, Vol. 7, No. 7, 5834–5841, 2013.

[197] Shimanoe, K., S. Endo, T. Matsuyama, K. Wada, and K. Okamoto, "Localized surface plasmon resonance in deep ultraviolet region below 200 nm using a nanohemisphere on mirror structure," *Scientific Reports*, Vol. 11, No. 1, 5169, 2021.

[198] Jha, S. K., Z. Ahmed, M. Agio, Y. Ekinci, and J. F. Löffler, "Deep-UV surface-enhanced resonance Raman scattering of adenine on aluminum nanoparticle arrays," *Journal of the American Chemical Society*, Vol. 134, No. 4, 1966–1969, 2012.

[199] Dubey, A., R. Mishra, C.-W. Cheng, Y.-P. Kuang, S. Gwo, and T.-J. Yen, "Demonstration of a superior deep-UV surface-enhanced resonance Raman scattering (SERRS) substrate and single-base mutation detection in oligonucleotides," *Journal of the American Chemical Society*, Vol. 143, No. 46, 19 282–19 286, 2021.

[200] Giordano, A. N. and R. Rao, "Beyond the visible: A review of ultraviolet surface-enhanced Raman scattering substrate compositions, morphologies, and performance," *Nanomaterials*, Vol. 13, No. 15, 2177, 2023.

[201] Kikawada, M., A. Ono, W. Inami, and Y. Kawata, "Plasmon-enhanced autofluorescence imaging of organelles in label-free cells by deep-ultraviolet excitation," *Analytical Chemistry*, Vol. 88, No. 2, 1407–1411, 2016.

[202] Crosbie, S. and D. Zerulla, "Long range surface plasmon resonance and enhanced fluorescence near the ultra-violet vacuum cutoff limit," *Journal of Applied Physics*, Vol. 111, No. 8, 084702, 2012.

[203] Tariq, Z. and R. Barthwal, "Affinity of anticancer drug daunomycin toward Tetrahymena telomeric G-quadruplex DNA D-[GGGG(TTGGGG)3]," *ACS Omega*, Vol. 4, No. 4, 6347–6359, 2019.

[204] Papp, L. A., M. Foroughbakhshfasaei, B. Fiser, P. Horváth, E. Kiss, K. Sekkoum, A. Gyéresi, G. Hancu, B. Noszál, Z.-I. Szabó, and G. Tóth, "Reversed-phase hplc enantioseparation of pantoprazole using a teicoplanin aglycone stationary phase — Determination of the enantiomer elution order using HPLC-CD analyses," *Chirality*, Vol. 32, No. 2, 158–167, 2020.

[205] Greenfield, N. J., "Using circular dichroism spectra to estimate protein secondary structure," *Nature Protocols*, Vol. 1, No. 6, 2876–2890, 2007.

[206] Jeong, H.-H., A. G. Mark, and P. Fischer, "Magnesium plasmonics for UV applications and chiral sensing," *Chemical Communications*, Vol. 52, No. 82, 12 179–12 182, 2016.

[207] Wang, Y., E. M. Peterson, J. M. Harris, K. Appusamy, S. Guruswamy, and S. Blair, "Magnesium as a novel UV plasmonic material for fluorescence decay rate engineering in free solution," *The Journal of Physical Chemistry C*, Vol. 121, No. 21, 11 650–11 657, 2017.

[208] Li, R., S. Xie, L. Zhang, L. Li, D. Kong, Q. Wang, R. Xin, X. Sheng, L. Yin, C. Yu, *et al.*, "Soft and transient magnesium plasmonics for environmental and biomedical sensing," *Nano Research*, Vol. 11, 4390–4400, 2018.

[209] Ren, B., X.-F. Lin, Z.-L. Yang, G.-K. Liu, R. F. Aroca, B.-W. Mao, and Z.-Q. Tian, "Surface-enhanced Raman scattering in the ultraviolet spectral region: UV-SERS on rhodium and ruthenium electrodes," *Journal of the American Chemical Society*, Vol. 125, No. 32, 9598–9599, 2003.

[210] Watson, A. M., X. Zhang, R. A. de La Osa, J. M. Sanz, F. González, F. Moreno, G. Finkelstein, J. Liu, and H. O. Everitt, "Rhodium nanoparticles for ultraviolet plasmonics," *Nano Letters*, Vol. 15, No. 2, 1095–1100, 2015.

[211] Zhang, X., P. Li, A. Barreda, Y. Gutiérrez, F. González, F. Moreno, H. O. Everitt, and J. Liu, "Size-tunable rhodium nanostructures for wavelength-tunable ultraviolet plasmonics," *Nanoscale Horizons*, Vol. 1, No. 1, 75–80, 2016.

[212] Kumar, G. and R. K. Soni, "Rhodium concave nanocubes and nanoplates as deep-UV resonant SERS platform," *Journal of Raman Spectroscopy*, Vol. 53, No. 11, 1890–1903, 2022.

[213] Roy, P., S. Zhu, J.-B. Claude, J. Liu, and J. Wenger, "Ultraviolet resonant nanogap antennas with rhodium nanocube dimers for enhancing protein intrinsic autofluorescence," *ACS Nano*, Vol. 17, No. 22, 22 418–22 429, 2023.

[214] Magnan, F., J. Gagnon, F.-G. Fontaine, and D. Boudreau, "Indium@silica core-shell nanoparticles as plasmonic enhancers of molecular luminescence in the UV region," *Chemical Communications*, Vol. 49, No. 81, 9299–9301, 2013.

[215] Kumamoto, Y., Y. Saito, A. Taguchi, M. Honda, K. Watanabe, and S. Kawata, "Indium for deep-UV plasmonics: Surface-enhanced Raman scattering," in *JSAP-OSA Joint Symposia, JSAP 2014*, 2818, Sapporo, Hokkaido, Japan, 2014.

[216] Yang, Y., J. M. Callahan, T.-H. Kim, A. S. Brown, and H. O. Everitt, "Ultraviolet nanoplasmonics: A demonstration of surface-enhanced Raman spectroscopy, fluorescence, and photodegradation using gallium nanoparticles," *Nano Letters*, Vol. 13, No. 6, 2837–2841, 2013.

[217] Marín, A. G., M. J. Hernández, E. Ruiz, J. M. Abad, E. Lorenzo, J. Piqueras, and J. L. Pau, "Immunosensing platform based on gallium nanoparticle arrays on silicon substrates," *Biosensors and Bioelectronics*, Vol. 74, 1069–1075, 2015.

[218] Marín, A. G., T. García-Mendiola, C. N. Bernabeu, M. J. Hernández, J. Piqueras, J. L. Pau, F. Pariente, and E. Lorenzo, "Gallium plasmonic nanoparticles for label-free DNA and single nucleotide polymorphism sensing," *Nanoscale*, Vol. 8, No. 18, 9842–9851, 2016.

[219] Dong, Z., T. Wang, X. Chi, J. Ho, C. Tserkezis, S. L. K. Yap, A. Rusydi, F. Tjiptoharsono, D. Thian, N. A. Mortensen, and J. K. W. Yang, "Ultraviolet interband plasmonics with Si nanostructures," *Nano Letters*, Vol. 19, No. 11, 8040–8048, 2019.

[220] He, Z., Z. Li, C. Li, W. Xue, and W. Cui, "Ultra-high sensitivity sensing based on ultraviolet plasmonic enhancements in semiconductor triangular prism meta-antenna systems," *Optics Express*, Vol. 28, No. 12, 17 595–17 610, 2020.

[221] Hopper, E. R., C. Boukouvala, J. Asselin, J. S. Biggins, and E. Ringe, "Opportunities and challenges for alternative nanoplasmonic metals: Magnesium and beyond," *The Journal of Physical Chemistry C*, Vol. 126, No. 26, 10 630–10 643, 2022.

[222] McMahon, J. M., G. C. Schatz, and S. K. Gray, "Plasmonics in the ultraviolet with the poor metals Al, Ga, In, Sn, Tl, Pb, and Bi," *Physical Chemistry Chemical Physics*, Vol. 15, 5415–5423, 2013.

[223] Zhu, L., Z. Li, and Y. Tian, "Lithography-free bismuth metamaterials for advanced light manipulation," *Photonics*, Vol. 10, No. 5, 602, 2023.

[224] Toudert, J. and R. Serna, "Ultraviolet-visible interband plasmonics with p-block elements," *Optical Materials Express*, Vol. 6, No. 7, 2434–2447, 2016.

[225] Gutiérrez, Y., R. A. de la Osa, D. Ortiz, J. M. Saiz, F. González, and F. Moreno, "Plasmonics in the ultraviolet with aluminum, gallium, magnesium and rhodium," *Applied Sciences*, Vol. 8, No. 1, 64, 2018.

[226] Sanz, J. M., D. Ortiz, R. A. de la Osa, J. M. Saiz, F. González, A. S. Brown, M. Losurdo, H. O. Everitt, and F. Moreno, "UV plasmonic behavior of various metal nanoparticles in the near- and far-field regimes: Geometry and substrate effects," *The Journal of Physical Chemistry C*, Vol. 117, No. 38, 19 606–19 615, 2013.

[227] Zorić, I., M. Zäch, B. Kasemo, and C. Langhammer, "Gold, platinum, and aluminum nanodisk plasmons: Material independence, subradiance, and damping mechanisms," *ACS Nano*, Vol. 5, No. 4, 2535–2546, 2011.

[228] Zhao, D., Z. Lin, W. Zhu, H. J. Lezec, T. Xu, A. Agrawal, C. Zhang, and K. Huang, "Recent advances in ultraviolet nanophotonics: From plasmonics and metamaterials to metasurfaces," *Nanophotonics*, Vol. 10, No. 9, 2283–2308, 2021.

[229] Biggins, J. S., S. Yazdi, and E. Ringe, "Magnesium nanoparticle plasmonics," *Nano Letters*, Vol. 18, No. 6, 3752–3758, 2018.

[230] Jeong, H.-H., A. G. Mark, M. Alarcón-Correa, I. Kim, P. Oswald, T.-C. Lee, and P. Fischer, "Dispersion and shape engineered plasmonic nanosensors," *Nature Communications*, Vol. 7, No. 1, 11331, 2016.

[231] Ringe, E., "Shapes, plasmonic properties, and reactivity of magnesium nanoparticles," *The Journal of Physical Chemistry C*, Vol. 124, No. 29, 15 665–15 679, 2020.

[232] Cheng, X., E. Lotubai, M. Rodriguez, and Y. Wang, "UV fluorescence enhancement by aluminum and magnesium equilateral bowtie nanoantennas," *OSA Continuum*, Vol. 3, No. 12, 3300–3313, 2020.

[233] Fievet, F., J. P. Lagier, B. Blin, B. Beaudoin, and M. Figlarz, "Homogeneous and heterogeneous nucleations in the polyol process for the preparation of micron and submicron size metal particles," *Solid State Ionics*, Vol. 32, 198–205, 1989.

[234] Ross, M. B. and G. C. Schatz, "Aluminum and indium plasmonic nanoantennas in the ultraviolet," *The Journal of Physical Chemistry C*, Vol. 118, No. 23, 12 506–12 514, 2014.

[235] Mishra, H., A. Dragan, and C. D. Geddes, "UV to NIR surface plasmon coupled and metal-enhanced fluorescence using indium thin films: Application to intrinsic (Label-less) protein fluorescence detection," *The Journal of Physical Chemistry C*, Vol. 115, No. 35, 17 227–17 236, 2011.

[236] Das, R. and R. K. Soni, "Synthesis and surface-enhanced Raman scattering of indium nanotriangles and nanowires," *RSC Advances*, Vol. 7, No. 51, 32 255–32 263, 2017.

[237] Gutiérrez, Y., P. García-Fernández, J. Junquera, A. S. Brown, F. Moreno, and M. Losurdo, "Polymorphic gallium for active resonance tuning in photonic nanostructures: From bulk gallium to two-dimensional (2D) gallenene," *Nanophotonics*, Vol. 9, No. 14, 4233–4252, 2020.

[238] Knight, M. W., T. Coenen, Y. Yang, B. J. M. Brenny, M. Losurdo, A. S. Brown, H. O. Everitt, and A. Polman, "Gallium plasmonics: Deep subwavelength spectroscopic imaging of single and interacting gallium nanoparticles," *ACS Nano*, Vol. 9, No. 2, 2049–2060, 2015.

[239] Horák, M., V. Čalkovský, J. Mach, V. Křápek, and T. Šikola, "Plasmonic properties of individual gallium nanoparticles," *The Journal of Physical Chemistry Letters*, Vol. 14, No. 8, 2012–2019, 2023.

[240] Wu, P. C., C. G. Khoury, T.-H. Kim, Y. Yang, M. Losurdo, G. V. Bianco, T. Vo-Dinh, A. S. Brown, and H. O. Everitt, "Demonstration of surface-enhanced Raman scattering by tunable, plasmonic gallium nanoparticles," *Journal of the American Chemical Society*, Vol. 131, No. 34, 12 032–12 033, 2009.

[241] Zhang, T., Y. Wang, K. Appusamy, B. Huang, J. Wang, F. Liu, S. Blair, S. Guruswamy, and A. Nahata, "Gallium platinum alloys — A new material system for UV plasmonics," *Optical Materials Express*, Vol. 7, No. 8, 2880–2887, 2017.

[242] Reineck, P., Y. Lin, B. C. Gibson, M. D. Dickey, A. D. Greentree, and I. S. Maksymov, "UV plasmonic properties of colloidal liquid-metal eutectic gallium-indium alloy nanoparticles," *Scientific Reports*, Vol. 9, No. 1, 5345, 2019.

[243] Toudert, J., R. Serna, and M. J. de Castro, "Exploring the optical potential of nano-bismuth: Tunable surface plasmon resonances in the near ultraviolet-to-near infrared range," *The Journal of Physical Chemistry C*, Vol. 116, No. 38, 20 530–20 539, 2012.

[244] Toudert, J., R. Serna, I. Camps, J. Wojcik, P. Mascher, E. Rebollar, and T. A. Ezquerra, "Unveiling the far infrared-to-ultraviolet optical properties of bismuth for applications in plasmonics and nanophotonics," *The Journal of Physical Chemistry C*, Vol. 121, No. 6, 3511–3521, 2017.

[245] Leng, D., T. Wang, Y. Li, Z. Huang, H. Wang, Y. Wan, X. Pei, and J. Wang, "Plasmonic bismuth nanoparticles: Thiolate pyrolysis synthesis, size-dependent LSPR property, and their oxidation behavior," *Inorganic Chemistry*, Vol. 60, No. 22, 17 258–17 267, 2021.

[246] Martínez-Lara, D. E., R. González-Campuzano, and D. Mendoza, "Bismuth plasmonics in the visible spectrum using texturized films," *Photonics and Nanostructures — Fundamentals and Applications*, Vol. 52, 101058, 2022.

[247] Piccinotti, D., B. Gholipour, J. Yao, K. F. Macdonald, B. E. Hayden, and N. I. Zheludev, "Compositionally controlled plasmonics in amorphous semiconductor metasurfaces," *Optics Express*, Vol. 26, No. 16, 20 861–20 867, 2018.

[248] Ou, J.-Y., J.-K. So, G. Adamo, A. Sulaev, L. Wang, and N. I. Zheludev, "Ultraviolet and visible range plasmonics in the topological insulator Bi1.5Sb0.5Te1.8Se1.2," *Nature Communications*, Vol. 5, No. 1, 5139, 2014.

[249] Law, S., V. Podolskiy, and D. Wasserman, "Towards nano-scale photonics with micro-scale photons: The opportunities and challenges of mid-infrared plasmonics," *Nanophotonics*, Vol. 2, No. 2, 103–130, 2013.

[250] Zhong, Y., S. D. Malagari, T. Hamilton, and D. M. Wasserman, "Review of mid-infrared plasmonic materials," *Journal of Nanophotonics*, Vol. 9, No. 1, 093791, 2015.

[251] Taliercio, T. and P. Biagioni, "Semiconductor infrared plasmonics," *Nanophotonics*, Vol. 8, No. 6, 949–990, 2019.

[252] Biagioni, P., J. Frigerio, A. Samarelli, K. Gallacher, L. Baldassarre, E. Sakat, E. Calandrini, R. W. Millar, V. Giliberti, G. Isella, D. J. Paul, and M. Ortolani, "Group-IV midinfrared plasmonics," *Journal of Nanophotonics*, Vol. 9, No. 1, 093789, 2015.

[253] Ginn, J. C., R. L. Jarecki, E. A. Shaner, and P. S. Davids, "Infrared plasmons on heavily-doped silicon," *Journal of Applied Physics*, Vol. 110, No. 4, 043110, 2011.

[254] Cada, M., D. Blazek, J. Pistora, K. Postava, and P. Siroky, "Theoretical and experimental study of plasmonic effects in heavily doped gallium arsenide and indium phosphide," *Optical Materials Express*, Vol. 5, No. 2, 340–352, 2015.

[255] Panah, M. E. A., O. Takayama, S. V. Morozov, K. E. Kudryavtsev, E. S. Semenova, and A. V. Lavrinenko, "Highly doped InP as a low loss plasmonic material for mid-IR region," *Optics Express*, Vol. 24, No. 25, 29 077–29 088, 2016.

[256] Law, S., D. C. Adams, A. M. Taylor, and D. Wasserman, "MidIR designer metals," *Optics Express*, Vol. 20, 12 155–12 165, 2012.

[257] Law, S., L. Yu, and D. Wasserman, "Epitaxial growth of engineered metals for mid-infrared plasmonics," *Journal of Vacuum Science & Technology B*, Vol. 31, No. 3, 03C121, 2013.

[258] Law, S., L. Yu, A. Rosenberg, and D. Wasserman, "All-semiconductor plasmonic nanoantennas for infrared sensing," *Nano Letters*, Vol. 13, No. 9, 4569–4574, 2013.

[259] Law, S., R. Liu, and D. Wasserman, "Doped semiconductors with band-edge plasma frequencies," *Journal of Vacuum Science & Technology B*, Vol. 32, No. 5, 052601, 2014.

[260] Neubrech, F., C. Huck, K. Weber, A. Pucci, and H. Giessen, "Surface-enhanced infrared spectroscopy using resonant nanoantennas," *Chemical Reviews*, Vol. 117, No. 7, 5110–5145, 2017.

[261] Poumirol, J.-M., C. Majorel, N. Chery, C. Girard, P. R. Wiecha, N. Mallet, R. Monflier, G. Larrieu, F. Cristiano, A.-S. Royet, *et al.*, "Hyper-doped silicon nanoantennas and metasurfaces for tunable infrared plasmonics," *ACS Photonics*, Vol. 8, No. 5, 1393–1399, 2021.

[262] Baldassarre, L., E. Sakat, J. Frigerio, A. Samarelli, K. Gallacher, E. Calandrini, G. Isella, D. J. Paul, M. Ortolani, and P. Biagioni, "Midinfrared plasmon-enhanced spectroscopy with germanium antennas on silicon substrates," *Nano Letters*, Vol. 15, No. 11, 7225–7231, 2015.

[263] Barho, F. B., F. Gonzalez-Posada, M.-J. Milla, M. Bomers, L. Cerutti, E. Tournié, and T. Taliercio, "Highly doped semiconductor plasmonic nanoantenna arrays for polarization selective broadband surface-enhanced infrared absorption spectroscopy of vanillin," *Nanophotonics*, Vol. 7, No. 2, 507–516, 2017.

[264] Milla, M. J., F. Barho, F. González-Posada, L. Cerutti, B. Charlot, M. Bomers, F. Neubrech, E. Tournie, and T. Taliercio, "Surface-enhanced infrared absorption with Si-doped InAsSb/GaSb nano-antennas," *Optics Express*, Vol. 25, No. 22, 26 651–26 661, 2017.

[265] Rodrigo, D., O. Limaj, D. Janner, D. Etezadi, *et al.*, "Mid-infrared plasmonic biosensing with graphene," *Science*, Vol. 349, No. 6244, 165–168, 2015.

[266] Farmer, D. B., P. Avouris, Y. Li, T. F. Heinz, and S.-J. Han, "Ultrasensitive plasmonic detection of molecules with graphene," *ACS Photonics*, Vol. 3, No. 4, 553–557, 2016.

[267] Zeng, K., C. Wu, X. Guo, F. Guan, Y. Duan, L. L. Zhang, X. Yang, N. Liu, Q. Dai, and S. Zhang, "Synthesized complex-frequency excitation for ultrasensitive molecular sensing," *eLight*, Vol. 4, No. 1, 1, 2024.

[268] Hu, H., X. Yang, X. Guo, K. Khaliji, S. R. Biswas, F. J. G. de Abajo, T. Low, Z. Sun, and Q. Dai, "Gas identification with graphene plasmons," *Nature Communications*, Vol. 10, No. 1, 1131, 2019.

[269] Bareza, N. J., K. K. Gopalan, R. Alani, B. Paulillo, and V. Pruneri, "Mid-infrared gas sensing using graphene plasmons tuned by reversible chemical doping," *ACS Photonics*, Vol. 7, No. 4, 879–884, 2020.

[270] Autore, M., P. Li, I. Dolado, F. J. Alfaro-Mozaz, R. Esteban, A. Atxabal, F. Casanova, L. E. Hueso, P. Alonso-González, J. Aizpurua, A. Y. Nikitin, *et al.*, "Boron nitride nanoresonators for phonon-enhanced molecular vibrational spectroscopy at the strong coupling limit," *Light: Science & Applications*, Vol. 7, No. 4, 17 172–17 178, 2018.

[271] Bylinkin, A., M. Schnell, M. Autore, F. Calavalle, P. Li, J. Taboada-Gutièrrez, S. Liu, J. H. Edgar, F. Casanova, L. E. Hueso, *et al.*, "Real-space observation of vibrational strong coupling between propagating phonon polaritons and organic molecules," *Nature Photonics*, Vol. 15, No. 3, 197–202, 2021.

[272] Bareza, N. J., B. Paulillo, T. M. Slipchenko, M. Autore, I. Dolado, S. Liu, J. H. Edgar, S. Vélez, L. Martín-Moreno, R. Hillenbrand, and V. Pruneri, "Phonon-enhanced mid-infrared CO2 gas sensing using boron nitride nanoresonators,"

ACS Photonics, Vol. 9, No. 1, 34–42, 2022.

[273] Bylinkin, A., F. Calavalle, M. Barra-Burillo, R. V. Kirtaev, E. Nikulina, E. Modin, E. Janzen, J. H. Edgar, F. Casanova, L. E. Hueso, *et al.*, "Dual-band coupling of phonon and surface plasmon polaritons with vibrational and electronic excitations in molecules," *Nano Letters*, Vol. 23, No. 9, 3985–3993, 2023.

[274] Qin, T., W. Ma, T. Wang, and P. Li, "Phonon polaritons in van der Waals polar heterostructures for broadband strong light-matter interactions," *Nanoscale*, Vol. 15, No. 28, 12 000–12 007, 2023.

[275] Folland, T. G., G. Lu, A. Bruncz, J. R. Nolen, M. Tadjer, and J. D. Caldwell, "Vibrational coupling to epsilon-near-zero waveguide modes," *ACS Photonics*, Vol. 7, No. 3, 614–621, 2020.

[276] Caldwell, J. D., A. V. Kretinin, Y. Chen, V. Giannini, M. M. Fogler, Y. Francescato, C. T. Ellis, J. G. Tischler, C. R. Woods, A. J. Giles, *et al.*, "Sub-diffractional volume-confined polaritons in the natural hyperbolic material hexagonal boron nitride," *Nature Communications*, Vol. 5, No. 1, 5221, 2014.

[277] Zhang, Q., Z. Zhen, Y. Yang, G. Gan, D. Jariwala, and X. Cui, "Hybrid phonon-polaritons at atomically-thin van der Waals heterointerfaces for infrared optical modulation," *Optics Express*, Vol. 27, No. 13, 18 585–18 600, 2019.

[278] Beliaev, L. Y., E. Shkondin, A. V. Lavrinenko, and O. Takayama, "Thickness-dependent optical properties of aluminum nitride films for mid-infrared wavelengths," *Journal of Vacuum Science & Technology A*, Vol. 39, No. 4, 043408, 2021.

[279] Beliaev, L. Y., E. Shkondin, A. V. Lavrinenko, and O. Takayama, "Thickness-dependent optical properties of aluminum nitride films for mid-infrared wavelengths," *Journal of Vacuum Science & Technology A*, Vol. 39, No. 4, 043408, 2021.

[280] McCarthy, D. E., "The reflection and transmission of infrared materials. V: Spectra from 2μ to 50μ," *Applied Optics*, Vol. 7, No. 10, 1997–2000, 1968.

[281] Nazempour, R., B. Zhang, Z. Ye, L. Yin, X. Lv, and X. Sheng, "Emerging applications of optical fiber-based devices for brain research," *Advanced Fiber Materials*, Vol. 4, 24–42, 2022.

[282] Munkhbat, B., P. Wróbel, T. J. Antosiewicz, and T. O. Shegai, "Optical constants of several multilayer transition metal dichalcogenides measured by spectroscopic ellipsometry in the 300–1700 nm range: High index, anisotropy, and hyperbolicity," *ACS Photonics*, Vol. 9, No. 7, 2398–2407, 2022.

[283] Kowalski, R. A., J. R. Nolen, G. Varnavides, S. M. Silva, J. E. Allen, C. J. Ciccarino, D. M. Juraschek, S. Law, P. Narang, and J. D. Caldwell, "Mid- to far-infrared anisotropic dielectric function of HfS2 and HfSe2," *Advanced Optical Materials*, Vol. 10, No. 23, 2200933, 2022.

[284] Pandey, P. S., S. K. Raghuwanshi, and S. Kumar, "Recent advances in two-dimensional materials-based Kretschmann configuration for SPR sensors: A review," *IEEE Sensors Journal*, Vol. 22, No. 2, 1069–1080, 2022.

[285] Mia, A. K., M. Meyyappan, and P. K. Giri, "Two-dimensional transition metal dichalcogenide based biosensors: From fundamentals to healthcare applications," *Biosensors*, Vol. 13, No. 2, 169, 2023.

[286] Sulleiro, M. V., A. Dominguez-Alfaro, N. Alegret, A. Silvestri, and I. J. Gómez, "2D materials towards sensing technology: From fundamentals to applications," *Sensing and Bio-Sensing Research*, Vol. 38, 100540, 2022.

[287] Grigorenko, A. N., M. Polini, and K. S. Novoselov, "Graphene plasmonics," *Nature Photonics*, Vol. 6, No. 11, 749–758, 2012.

[288] Low, T. and P. Avouris, "Graphene plasmonics for terahertz to mid-infrared applications," *ACS Nano*, Vol. 8, No. 2, 1086–1101, 2014.

[289] De Abajo, F. J. G., "Graphene plasmonics: Challenges and opportunities," *ACS Photonics*, Vol. 24, 135–152, 2014.

[290] Han, Z. and S. I. Bozhevolnyi, "Radiation guiding with surface plasmon polaritons," *Reports on Progress in Physics*, Vol. 76, No. 1, 016402, 2013.

[291] Chen, J., M. Badioli, P. Alonso-González, S. Thongrattanasiri, F. Huth, J. Osmond, M. Spasenović, A. Centeno, A. Pesquera, P. Godignon, A. Z. Elorza, N. Camara, F. J. G. de Abajo, R. Hillenbrand, and F. H. L. Koppens, "Optical nano-imaging of gate-tunable graphene plasmons," *Nature*, Vol. 487, No. 7405, 77–81, 2012.

[292] Takayama, O. and A. V. Lavrinenko, "Optics with hyperbolic materials," *Journal of the Optical Society of America B*, Vol. 36, No. 8, F38–F48, 2019.

[293] Dai, S., Q. Ma, M. K. Liu, T. Andersen, Z. Fei, M. D. Goldflam, M. Wagner, K. Watanabe, T. Taniguchi, M. Thiemens, *et al.*, "Graphene on hexagonal boron nitride as a tunable hyperbolic metamaterial," *Nature Nanotechnology*, Vol. 10, No. 8, 682–686, 2015.

[294] Chen, S., M. Autore, J. Li, P. Li, P. Alonso-Gonzalez, Z. Yang, L. Martin-Moreno, R. Hillenbrand, and A. Y. Nikitin, "Acoustic graphene plasmon nanoresonators for field-enhanced infrared molecular spectroscopy," *ACS Photonics*, Vol. 4, No. 12, 3089–3097, 2017.

[295] Brar, V. W., M. S. Jang, M. Sherrott, J. J. Lopez, and H. A. Atwater, "Highly confined tunable mid-infrared plasmonics in graphene nanoresonators," *Nano Letters*, Vol. 13, No. 6, 2541–2547, 2013.